SWING domains prime chromatin for nuclear body–mediated gene regulation

Ruofan Yu, Abhisha Sawant Dessai, Hanna Sas-Nowosielska, Amal Oubarri, Hannah Kim, Christine Faunce, Benjamin Vanderkruk, Katherine A Alexander, Son C Nguyen, Ian D. Krantz, Eric F Joyce, Melike Lakadamyali and Shelley L Berger

Abstract

Nuclear speckles have long been recognized as RNA-rich nuclear bodies, yet their role in genome organization and gene regulation remains incompletely understood. Using a rapid dTAG-mediated degradation system to simultaneously deplete SON and SRRM2—the core structural components of nuclear speckles—we identify a novel class of genomic regions, which we term SWING domains. Upon speckle disruption, SWING domains relocate to the nuclear periphery and acquire repressive histone marks such as H3K9me3, accompanied by transcriptional downregulation, particularly of genes involved in developmental pathways. Notably, human mutations in SON and SRRM2 are associated with neurodevelopmental disorders characterized by intellectual disability and global developmental delay. Patient-derived cells bearing such mutations similarly exhibit SWING-domain relocalization and gene repression, underlining a role for speckles in developmental gene regulation. We also report that previously discovered drug-induced speckle rejuvenation can partially rescue aberrant SWING-domain localization to the nuclear lamina and the associated transcriptome in patient-derived cells. These findings establish nuclear speckles as key organizers of active chromatin, functioning in opposition to repressive compartments like the nuclear lamina. Our work reveals a mechanism for how nuclear bodies contribute to 3D genome organization and highlights the importance of nuclear speckles in developmental regulation, providing potential avenues for therapeutic intervention.

Impact Statement:

1. Identification of nuclear speckles as determinants of specific 3D genome features.
2. Demonstration of functional interactions between opposing nuclear compartments through SWING domains.
3. Establishes developmental relevance of speckle-mediated genome organization.
4. Provides potential avenues for therapeutic intervention in speckleopathies.

Introduction

Nuclear bodies are membraneless, morphologically distinct sub-nuclear compartments increasingly recognized as active participants in genome function rather than passive storage depots. Among them, nuclear speckles are enriched for RNAs and RNA-processing proteins and have been implicated in both chromosome organization and gene regulation[1,2]. In parallel with broader efforts to integrate structure and function in the 4D nucleome, evidence has accumulated that speckles help coordinate transcription, splicing, 3′-end formation, and mRNA export, positioning them as dynamic hubs for gene expression[3,4].

Genomic mapping of speckles[5–8] showed that genomic regions closest to speckles—so-called speckle-associated domains (SPADs)—harbor dense clusters of actively transcribed genes and exhibit euchromatic features, including H3K27ac and H3K4me3 enrichment and robust RNA polymerase II occupancy; importantly, mean distance to speckles is a strong predictor of expression across cell types[6]. Consistent imaging and genomic analyses emphasize that speckle proximity marks transcriptionally permissive neighborhoods enriched for RNA-processing machinery and active histone modifications[5–8]. In contrast, lamina-associated domains (LADs) are depleted of active marks, enriched for repressive heterochromatin (for example, H3K9me3-associated states), and display low gene activity, underscoring a spatial and epigenetic opposition between speckle-proximal and lamina-proximal compartments[9,10]. Despite this mutual exclusivity, how the compartments are stably demarcated and whether there is an active competition between them, is not known.

Further, although there is striking correlation between SPADs and active chromatin[5–8] , mechanistic insight into how speckles contribute to chromatin organization remains lacking. Our previous work implicated chromatin architectural factors—CTCF and the cohesin subunit RAD21—in promoting speckle–chromatin association, providing evidence that speckles participate in 3D genome architecture[8] . However, relatively few perturbation studies have directly tested speckle function in active chromatin organization, and those available have generally reported only modest effects on chromatin architecture[11,12], a confounding outcome that suggests it may be necessary to look beyond active chromatin to uncover how speckles exert broad organizational roles.

It is notable that speckles appear to have profound relevance to human health. The clinical relevance of speckle integrity is highlighted by “nuclear speckleopathies”: inherited human variants in core speckle components[13] , including in SON[14] and SRRM2[15] , are associated with neurodevelopmental disorders. Severe speckleopathies are characterized by intellectual disability and global developmental delay, underscoring the importance of speckles to normal human development[16].

Here, we acutely disrupt speckles via rapid dTAG-mediated co-degradation of SON and SRRM2 to map consequences for genome organization and transcription. We define a speckle-wired genomic program and reveal a class of domains that, upon speckle disruption, relocalize to the nuclear lamina, acquire repressive chromatin features, and undergo transcriptional downregulation—particularly among developmental genes. Analyses in patient-derived cells bearing SON mutation expose concordant domain relocalization and gene repression, thus linking speckle integrity to developmental gene control. Finally, we show that pharmacologic “speckle rejuvenation” can partially rescue aberrant domain localization and transcription, suggesting potential for therapeutic intervention in speckle-associated pathologies.

Results

1. Disruption of nuclear speckles leads to increased lamina association of certain genomic domains

The core nuclear speckle components SON and SRRM2—both necessary for speckle formation[13] —are required for cell and organismal viability[17,18]. To enable temporal control of speckle disruption, we used a previously constructed K562 cell line in which both SON and SRRM2 were tagged with FKBP12, allowing acute depletion with the small molecule dTAG[11]. Depletion of both proteins was evident by 6 h of dTAG treatment and persisted for at least 24 h (Figure 1A). Nuclear speckles were effectively dispersed after 24 h of dTAG treatment; proteins normally enriched in speckles, including RBM25[19,20] and SF3a66[7] , lost their speckle-like localization and redistributed throughout the nucleoplasm with reduced granularity and more uniform distribution (Supplementary Figure 1A).

To assess changes in chromatin organization upon speckle disruption, we performed STORM (Stochastic Optical Reconstruction Microscopy) imaging of immunolabeled total histone H3. H3 protein levels remain unchanged following dTag treatment to deplete SON/SRRM2 (Supplementary Figure 1B). We observed striking redistribution of H3 toward the nuclear periphery. To quantify the changes in chromatin organization in an unbiased fashion, we applied O-SNAP[21,22] (Objective Single Molecule Nuclear Architecture Profiler)[21] analysis to extract 144 features representing the spatial distribution of chromatin domains within the nucleus from the STORM H3 images. This analysis revealed significant changes to chromatin domain organization at the nuclear periphery (see Supplementary Figure 1C for all imaged nuclei and summary of O-SNAP significant features), including a significant increase of the thickness of Lamin Associated Domains (LADs) modeled from the STORM images of chromatin at the nuclear periphery (Figure 1B). This analysis is consistent with increased association of chromatin with lamina-associated domains (LADs), however, with no apparent change in nuclear size (Figure 1C).

In light of this observation—that speckle disruption relocates chromatin to the lamina—we investigated whether the effect is global or confined to specific genomic regions via assaying DNA association with the lamina utilizing Lamin B1 CUT&RUN[23]. Our Lamin B1 CUT&RUN profiles showed strong technical reproducibility (Supplementary Figure 2A) and correlated well with previous Lamin B1 DamID[24], a widely used method for mapping lamina-associated regions (Supplementary Figure 2B). We also note that Lamin B1 subcellular localization and protein level were not visibly altered in 24h dTAG-treated cells (Supplementary Figure 2C). Upon 24 h of dTAG treatment, we observed striking gains of Lamin B1 association with specific DNA regions, rather than a global increase (Figure 1D–E). Given the sensitivity of these regions to speckle disruption, we term them SWING domains (see purple region of BED tracks in Figure 1D–E). Consistent with the genome browser tracks, the metagene plot and heat map show a clear increase in lamina association, represented by an increase of Lamin B1 CUT&RUN signal, within SWING domains (Figure 1F), but not within canonical LADs or speckle-associated domains (SPADs). To further substantiate this conclusion, we performed DNA-FISH to measure the distance between probe foci and the nuclear periphery. In agreement with the Lamin B1 CUT&RUN results, SWING probes relocated significantly closer to the lamina, whereas SPAD probes showed no significant movement (Figure 1G-H). In summary, we observed that a subfraction of the genome—here termed SWING domains—relocates to the nuclear lamina upon acute disruption of nuclear speckles.

2. SWING domains exhibit intermediate properties

We next investigated certain properties of SWING domains. Using previously published genomic maps of speckles (SON TSA-seq) and the nuclear lamina (Lamin B1 DamID) in K562 cell[6,24] , we found that SWING domains exhibit intermediate association level with both structures, indicating SWING is located between speckles and nuclear lamina (Figure 2A–C). To assess whether this conclusion holds cytologically, we analyzed genome-wide multiplex FISH (MERFISH) data generated in IMR90 cells[25]. Although this is a different cell line, prior work reported some conservation of both SPADs and LADs across cell lines[6,10,26] . Consistent with the genomic profiles, SWING domains in the MERFISH dataset occupied intermediate distances to both speckles and the lamina (Figure 2D–F).

At broader genomic scale, lamina association shows partial conservation across cell lines, with a subset of lamina-associated domains (LADs) shared across cell types while other LADs are more dynamic[26]. Given the SWING domain sensitivity to speckle perturbation and its intermediate nature, we investigated whether the SWING domain is also more variable across cell lines. We compared published Lamin-B1 association profiles[24] for K562 (chronic myeloid leukemia), HFFc6 (human foreskin fibroblast), HCT116 (colorectal cancer), and H1 (human embryonic stem cell) cell lines. Lamin B1 association exhibited significantly higher variability (quantified as the standard deviation of the Lamin B1 signal across these four cell lines) in SWING domains compared with canonical LADs and SPADs (Figs 2G–2H), and, consistently, the majority of medium- to high-variability Lamin B1–associated domains across these cell types reside within SWING domains (Figure 2I).

We next asked whether SWING domains also display intermediate chromatin architecture. Because SPADs are strongly associated with the active A1 subcompartment[5,27] and LADs with the repressive B2/B3 subcompartment[27] , we examined subcompartment composition within SWING domains. Using published Hi-C data from K562 cells[28] , we assigned genomic subcompartments[29] and observed that SWING domains frequently co-occur with the intermediate A2 and B1 subcompartments (Figure 2J). Genome-wide analyses further revealed that SWING domains are enriched for A2 and B1, whereas both SPADs and LADs are depleted for these intermediate subcompartments (Figure 2K–L). Thus, even when considering chromatin partitioning alone, independent of lamina or speckle association, SWING domains exhibit intermediate properties that are distinct from LADs and SPADs, suggesting a unique biological role.

3. SWING domain becomes more heterochromatin-like upon speckle disruption

Given that SWING domains show intermediate association with the nuclear lamina and nuclear speckles, we next investigated whether they also display hybrid histone modification profiles, between activation-associated acetylation and repression-associated methylation. Using publicly available ENCODE ChIP–seq datasets[30] from K562 cells, we quantified the distribution of six histone modifications (Figure 3A). For all six modifications, SWING domains showed signal levels between those observed in LADs and SPADs. Notably, SWING regions exhibited intermediate enrichment for the facultative heterochromatin mark H3K27me3 and the constitutive heterochromatin mark H3K9me3 (Figure 3A). These two modifications form an interlaced pattern within SWING domains, in contrast to the more uniform distribution of H3K27me3 in SPADs and H3K9me3 in LADs (sample region in Figure 3B). Together, these patterns indicate that SWING domains represent an intermediate chromatin state bridging constitutive and facultative heterochromatin.

We next examined whether acute speckle disruption alters H3K27me3 and H3K9me3 distribution. Immunofluorescence in cells with or without dTAG-mediated speckle disruption showed that H3K27me3 remained broadly evenly dispersed across the nucleus, whereas H3K9me3 redistributed toward the nuclear periphery (Figure 3C; quantification in Figure 3D). Because SWING domains relocalize to the nuclear lamina—a nuclear context associated with H3K9me3 deposition—we examined whether these changes occur specifically within SWING. We utilized CUT&RUN profiling for H3K27me3 and H3K9me3 and focused on the SWING set defined previously (Figure 1). There was a decrease in H3K27me3 at both SWING and SPAD (example tracks in Figure 3E; genome-wide quantification in Figure 3F) and, in contrast, an increase in H3K9me3 that was specific to SWING (Figure 3E, G). Beyond changes in signal magnitude, most regions with significant gained H3K9me3 mapped to SWING (Figure 3H, left), yielding a clear enrichment (Figure 3I). We also detected an enrichment for depleted H3K27me3 across SWING, albeit weaker than for gained H3K9me3 (Figure 3H, right; Figure 3I). Together, the increased H3K9me3 and reduced H3K27me3 indicate that, upon acute speckle disruption, SWING chromatin shifts towards a constitutive heterochromatin-like state.

4. Nuclear Speckle Disruption leads to down-regulation of SWING genes

We investigated whether the increased lamina association and gain of repressive H3K9me3 in SWING domains upon acute speckle depletion correlates with acquisition of gene repression. We performed RNA-seq in K562 cells with 24 h of dTAG treatment to disrupt nuclear speckles or control. As quality control, we observed a general shift toward downregulation in dTAG-treated samples (Supplementary 3A). We report that LADs, SWING, and SPADs show increasing numbers of expressed genes and increasing basal expression (Supplementary 3B), consistent with previous observations that gene expression increases with speckle association and decreases with lamina association[5] . Consistent with prior reports that speckles promote expression of speckle-associated genes[7,8,31,32] , genes in SPADs were predominantly downregulated upon speckle disruption (Figure 4A-B). Strikingly, genes in SWING domains were also significantly downregulated, and to an even greater extent than were SPAD genes (Figure 4A-B). This difference was not explained by baseline expression: in an expression-matched analysis, SWING genes still showed a stronger tendency toward downregulation than SPAD genes (Figure 4C). SWING-domain genes formed a distinct cluster among differentially expressed genes in both the volcano plot and hierarchical clustering in comparison with SPAD genes (Figure 4D–E). Genome browser views further illustrate these trends: genes with increased Lamin B1 CUT&RUN signal tended to be downregulated, particularly within SWING domains (e.g., LINC02794 and CYP39A1), whereas genes in regions without increased Lamin B1 were unchanged or upregulated (e.g., FAAH and POLH) (Figure 4F). Of note, because very few LAD genes are expressed in these cells, they were excluded from this comparison.

Beyond the well-documented role of speckles in promoting transcription of SPAD genes, our data indicate that speckles also regulate genes in SWING domains, which lie at intermediate distances from speckles, potentially via a distinct mechanism. Because SPAD genes are enriched in cellular processes requiring high basal and/or rapid expression[6,33] (e.g., housekeeping and stress-response pathways), we investigated whether genes within SWING domains also encompass preferential pathway associations. Motif analysis across all identified SWING domain revealed that top-ranked transcription factors enriched include developmental regulators, such as the embryonic and cell-fate determinant SOX7[34] and the homeobox factor SIX1[35] (Figure 4G). Consistently, gene ontology analysis of SWING-localized genes showed significant enrichment for development-related pathways (Supplementary 3C). In addition, genes downregulated upon acute speckle disruption were significantly enriched for nervous system and circulatory system development terms (Figure 4H). Together, these results suggest that, in contrast to SPAD genes that require high basal and/or rapid expression, SWING genes are subject to developmentally induced activation or repression and are particularly sensitive to speckle-mediated control, potentially enabling finer spatial and temporal regulation characteristic of developmental programs.

5. SWING domains relocate away from the lamina upon LMNA disruption

Building on our finding that SWING domains relocalize toward the nuclear lamina after speckle disruption—accompanied by increased H3K9me3 and gene downregulation—we investigated whether speckles and the lamina might actually "compete" for association at SWING domains. Prior studies suggest that speckle- and lamina-associated chromatin are largely mutually exclusive[24,27], raising a question of whether "swinging" occurs bidirectionally, in particular whether weakening the nuclear lamina tethering relocates SWING domains away from the lamina and potentially toward speckles.

Lamina association is mediated predominantly by two factors, the Lamin B receptor (LBR) and Lamin A/C (LMNA), which engage distinct tethering mechanisms[36]. Although their genome-wide occupancy is broadly similar[37] , perturbation studies show factor-specific sensitivity: LBR loss tends to cause widespread LAD detachment, whereas LMNA loss appears, on average, milder[24]. To test how each factor affects SWING domain localization, we reanalyzed published Lamin B1 DamID datasets from K562 cells bearing

CRISPR-mediated knockouts of LBR or LMNA[24], using the LAD/SWING/SPAD annotations defined with our double dTAG system. We observed that LMNA knockout produced a selective reduction of lamina association in SWING domains, with minimal change across canonical LADs or SPADs (Figure 5A; genome-wide summary in Figure 5B). In contrast, LBR knockout caused a global decrease in lamina association across LADs but a relative increase in lamina association within SWING domains (Figure 5A–B). A differential analysis of Lamin B1 signal confirmed that most regions changing in LMNA mutants map to SWING, and these changes are directionally opposite in LMNA versus LBR backgrounds (heatmap of all differential bins in Figure 5C; genome wide quantification in Figure 5D). Together, these results indicate that, among the two lamina tethering factors, LMNA specifically counterbalances speckle association at SWING domains, while LBR primarily maintains broad LAD tethering.

We investigated whether these localization changes translate into altered gene expression. Consistent with the localization shift, genes located in regions that show a significant decrease in Lamin B1 association in LMNA reduction were downregulated upon speckle disruption (Figure 5E, dTAG; see Figure 5F for representative Lamin B1 DamID and RNA-seq coverage). However, these genes were significantly upregulated only in the LMNA mutant (Figure 5E, LMNA; p-values from one-sample tests against zero are shown), with no significant change in the LBR mutant (Figure 5E, LBR). These inverse effects support a competitive model in which speckles and LMNA establishing opposite regulatory influences on SWING-domain genes. In summary, our data support a bidirectional "swinging" of SWING domains between speckles and the lamina: speckle disruption relocates SWING domains toward the lamina, leading to gene repression, whereas LMNA loss relocates SWING domains away from the lamina, leading to gene de-repression.

6. Speckle activation by drug treatment reduces lamina tethering

Hence, loss of lamina tethering, specifically via LMNA disruption, relocalizes SWING domains away from the nuclear lamina. We investigated whether a speckle gain-of-function would produce a similar outcome. A recent study identified the FDA-approved small molecule pyrvinium pamoate (PP) as a speckle gain-of-function treatment that increases speckle volume and mimics the transcriptional response of SON overexpression by lowering the surface tension of an intrinsically disordered region in SON[38]. Those findings demonstrate robust speckle enlargement in mouse embryonic fibroblasts and human iPSC-derived neurons. We tested this phenotype in K562 cells: PP treatment markedly increased both individual speckle size and speckle number for SON and the speckle-localized factor RBM25 (Figure 6A). Using STORM imaging, we further observed that cells treated with 100 nM PP, despite having similar nuclear size, exhibited a significant reduction in LAD thickness (Figure 6B–6C)—the exact opposite of the LAD thickening observed upon dTAG-mediated speckle disruption (Figure 1B–1C).

Mutations in the speckle core proteins SON and SRRM2 are associated with neurodevelopmental disorders; SON mutations cause Zhu–Tokita–Takenouchi–Kim (ZTTK) syndrome[14], and SRRM2 mutations are linked to a yet-unnamed developmental disorder[15]. Affected individuals show overlapping phenotypes, including developmental delay, distinctive facial features, and intellectual disability, supporting a hypothesis that speckle dysfunction can lead to a group of neurodevelopmental pathologies, or "nuclear speckleopathies"[16]. Our findings above reveal that speckles regulate SWING domains which are enriched for developmental pathways. Thus, we next investigated: (1) whether cells derived from patients with mutations in speckle genes exhibit aberrant gains in lamina association, and (2) whether pharmacological speckle activation can restore speckle morphology and function in these patient-derived cells. We analyzed a blood-derived lymphoblastoid cell line (LCL) from a patient carrying a premature stop-gain mutation in SON (P276; c.3334C>T; Sanger validation in Figure 6D; patient ontology terms in Supplementary 4A). Consistent with the genotype, SON expression in P276 was ~50% of control by RNA-seq (Supplementary 4B). Immunofluorescence revealed smaller and fewer nuclear speckles in P276 compared with a healthy

donor LCL (S1) (Figure 6E; quantification in Figure 6F–6G). We then treated cells with pyrvinium pamoate (PP) and found that speckle number and area in P276 were restored nearly to control levels (Figure 6F; S1 vs. P276+PP).

We performed Lamin B1 CUT&RUN in S1 and P276. Consistent with our K562 dTAG results (Figure 1), P276 showed aberrant increases in lamina association specifically within SWING domains, with little or no change across canonical LADs or SPADs (browser view in Figure 6H; genome-wide summary in Figure 6I). SWING domains identified in P276 significantly overlapped those defined in K562 (Figure 6J), and were similarly highly enriched of nervous system development pathway genes (Supplementary 4C). Notably, 100 nM PP treatment reduced the aberrant Lamin B1 association in P276 (example locus in Figure 6H; genome-wide summary in Figure 6I; heatmap of all laminB1 differential region in Figure 6M). Across all SWING domains in P276, nearly half were rescued by PP (Figure 6K), and reciprocally, the majority of PP-rescued regions fell within SWING (Figure 6L). In summary, patient cells harboring a disease-causing SON mutation exhibit abnormal increases in chromatin–lamina associations, manifesting within SWING domains, that are mitigated by PP treatment, consistent with speckle activation restoring both speckle morphology and lamina association toward a healthy state.

7. Developmental pathway dysregulation in speckleopathy patient cells is mitigated by pyrvinium pamoate

We next investigated whether the aberrant lamina association observed in the P276 patient line—and its partial reversal by PP—extends to transcriptional changes. We performed RNA-seq in LCLs from a healthy donor (S1) and from P276 (Supplementary 4D). Genes located within SWING domains (the regions showing aberrant lamina gain in P276) were overwhelmingly downregulated in P276 relative to S1 (distribution in Figure 7A; domain focused comparison in Figure 7B). Compared with SPAD genes—of which slightly more than half were significantly downregulated versus upregulated—more than 90% of SWING genes were downregulated (Figure 7C; heatmap in Figure 7D). These data mirror our acute speckle disruption results in K562 (Figure 4) and indicate that SWING genes are also highly sensitive to speckle mediated control in a patient context with long-term speckle dysfunction.

We next assessed whether PP treatment modulates gene expression at loci with aberrant lamina gain that were rescued at the chromatin level. Across genes in these PP-rescued regions, we observed a modest upward shift in expression (Figure 7E). Although the aggregate change did not reach statistical significance, the small number of expressed genes in this subset ($n = 47$) likely limits power. Focusing on genes meeting a stringent rescue criterion (significantly downregulated in P276 vs. S1 and significantly upregulated in P276+PP vs. P276 at FDR < 0.1), we identified several developmentally relevant genes, including the G protein–coupled receptor ADGRA3, the homeobox transcription factor MEIS2, and HDAC9, which is implicated in cardiac muscle development (example locus in Figure 7G). Gene ontology analysis of PP-rescued genes showed enrichment for nervous system development terms (Figure 7H). The overall magnitude of rescue was limited, which is expected because there is low baseline expression of developmental programs in K562 and LCL models, not undergoing differentiation, which constrain detection of robust transcriptional restoration.

Discussion

In this study, we identify a novel class of genomic regions—which we term SWING domains—that are sensitive to speckle dysfunction: either acute depletion in engineered cells or by clinical patient-derived mutations in speckle components relocates these domains towards the nuclear lamina. This repositioning is accompanied by increased H3K9me3 and preferential downregulation of genes residing in SWING domains, which are enriched for developmental pathways. We further show that nuclear lamina component

Lamin A competes with speckles for SWING positioning and regulation: Lamin A loss shifts SWING away from the lamina and induces the opposite transcriptional response, indicating inverse control by speckles and Lamin A. Finally, as proof of principle, pharmacological speckle activation with pyrvinium pamoate partially corrects both nuclear architecture—by reducing aberrant lamina association—and expression of a subset of developmentally relevant genes in patient cells. These findings suggest the possibility of drug-mediated modulation of nuclear body–chromatin interactions to mitigate specific consequences of speckle-related dysfunction (Figure 7I).

Our study identifies nuclear speckles as determinants of specific genome features and, for the first time, shows that disrupting speckles directly alters chromatin organization by increasing nuclear lamina association (Figure 1). Although speckles are long correlated with active chromatin, the evidence is largely correlational, with direct perturbation tests previously limited. Prior work used siRNA against SRRM2 in a mouse cell line[12] , or a 6-hour acute co-degradation of SON and SRRM2 followed by 3D-genome readouts (HiChIP)[11] ; in these studies there were minimal global changes in contacts. In contrast, we reveal that the effects of speckle disruption are not genome-wide but rather concentrated in a defined subset of regions—the SWING domains. This domain specificity, and the partial or short-term nature of earlier perturbations, likely explains limited changes detected previously.

Our results also demonstrate competition for chromatin association of SWING domains between nuclear speckles and the nuclear lamina (Figure 5). Building on the inverse correlation between speckle and lamina association observed across cell lines[6,27] , we show that this competition specifically involves speckles and lamin A/C—but not LBR— although lamin A/C and LBR are both major mediators of chromatin–lamina interactions. This is consistent with prior observations that lamin A/C–sensitive LADs are more facultative and variable, whereas LBR-dependent LADs are more constitutive[36,39]. Notably, lamin A/C can exist in a nucleoplasmic pool[40] , potentially regulated by phosphorylation[41] which could be relevant to the flux of SWING domains. Overall, the molecular mechanism underlying this competition remains to be determined.

We establish that, in addition to regulating speckle-associated (SPAD) genes, nuclear speckles also regulate non-speckle-associated genes within SWING domains via a distinct mechanism. Prior work shows that speckles facilitate expression of speckle-proximal genes such as p53 targets[31] and HIF-2α targets[32] , potentially by enhancing splicing efficiency[7]. Our results extend this model: speckles also compete with nuclear lamina mediated repression of non-speckle-associated SWING genes, limiting deposition of repressive marks such as H3K9me3 (Figure 3). We also find pathway differences between SWING domains and SPAD: SPAD genes are enriched for housekeeping and stress-response functions, whereas SWING domains appear to be enriched for developmental pathways (Figure 4G–H). We therefore hypothesize that, unlike SPAD genes that may require high basal and/or rapid expression, SWING genes could occupy an intermediate regulatory state that is particularly sensitive to speckle-mediated control, potentially enabling finer spatial and temporal regulation characteristic of developmental programs.

Multiple reports implicate mutations in nuclear speckle components, including SON and SRRM2 in neurodevelopmental disease[14–16]. In a clinical context using patient-derived cell lines, we observed that speckle dysfunction caused by naturally occurring mutations also led to aberrant lamina association, and correlated repression of SWING genes (Figure 6-7). We further found that treatment with pyrvinium pamoate (PP)—a small molecule drug reported to function by modifying biophysical properties of an intrinsically disordered region (IDR) of SON[38] —rescued aberrant lamina association and partially improved transcriptomic readouts. Although substantial work remains before clinical application, these results suggest fascinating potential therapeutic avenues: small-molecule drugs and other strategies to modulate the biophysical properties of nuclear body components—including peptides and nanobodies—could partially restore the function of affected nuclear bodies in disease contexts.

References

1. Spector, D. L. & Lamond, A. I. Nuclear Speckles. *Cold Spring Harb. Perspect. Biol.* **3**, a000646 (2011).

2. Galganski, L., Urbanek, M. O. & Krzyzosiak, W. J. Nuclear speckles: molecular organization, biological function and role in disease. *Nucleic Acids Res.* **45**, 10350–10368 (2017).

3. Consortium, 4D Nucleome *et al.* An integrated view of the structure and function of the human 4D nucleome. *bioRxiv* 2024.09.17.613111 (2024) doi:10.1101/2024.09.17.613111.

4. Faber, G. P., Nadav-Eliyahu, S. & Shav-Tal, Y. Nuclear speckles – a driving force in gene expression. *J. Cell Sci.* **135**, (2022).

5. Chen, Y. *et al.* Mapping 3D genome organization relative to nuclear compartments using TSA-Seq as a cytological ruler. *J. Cell Biol.* **217**, 4025–4048 (2018).

6. Zhang, L. *et al.* TSA-seq reveals a largely conserved genome organization relative to nuclear speckles with small position changes tightly correlated with gene expression changes. *Genome Res.* **31**, 251–264 (2021).

7. Bhat, P. *et al.* Genome organization around nuclear speckles drives mRNA splicing efficiency. *Nature* **629**, 1165–1173 (2024).

8. Yu, R. *et al.* CTCF/RAD21 organize the ground state of chromatin–nuclear speckle association. *Nat. Struct. Mol. Biol.* **32**, 1–12 (2025).

9. Guelen, L. *et al.* Domain organization of human chromosomes revealed by mapping of nuclear lamina interactions. *Nature* **453**, 948–951 (2008).

10. Steensel, B. van & Belmont, A. S. Lamina-Associated Domains: Links with Chromosome Architecture, Heterochromatin, and Gene Repression. *Cell* **169**, 780–791 (2017).

11. Roseman, S. A. *et al.* DNA methylation insulates genic regions from CTCF loops near nuclear speckles. *eLife* **13**, RP102930 (2025).

12. Hu, S., Lv, P., Yan, Z. & Wen, B. Disruption of nuclear speckles reduces chromatin interactions in active compartments. *Epigenetics Chromatin* **12**, 43 (2019).

13. Ilik, İ. A. *et al.* SON and SRRM2 are essential for nuclear speckle formation. *eLife* **9**, e60579 (2020).

14. Dingemans, A. J. M. *et al.* Establishing the phenotypic spectrum of ZTTK syndrome by analysis of 52 individuals with variants in SON. *Eur. J. Hum. Genet.* **30**, 271–281 (2022).

15. Cuinat, S. *et al.* Loss-of-function variants in SRRM2 cause a neurodevelopmental disorder. *Genet. Med.* **24**, 1774–1780 (2022).

16. Regan-Fendt, K. E. & Izumi, K. Nuclear speckleopathies: developmental disorders caused by variants in genes encoding nuclear speckle proteins. *Hum. Genet.* **143**, 529–544 (2024).

17. Arafeh, R., Shibue, T., Dempster, J. M., Hahn, W. C. & Vazquez, F. The present and future of the Cancer Dependency Map. *Nat. Rev. Cancer* **25**, 59–73 (2025).

18. Vukadin, L. *et al.* A mouse model of Zhu-Tokita-Takenouchi-Kim syndrome reveals indispensable SON functions in organ development and hematopoiesis. *JCI Insight* **9**, e175053 (2024).

19. Thul, P. J. *et al.* A subcellular map of the human proteome. *Science* **356**, (2017).

20. Zhou, A., Ou, A. C., Cho, A., Benz, E. J. & Huang, S.-C. Novel Splicing Factor RBM25 Modulates Bcl-x Pre-mRNA 5′ Splice Site Selection. *Mol. Cell. Biol.* **28**, 5924–5936 (2008).

21. Kim, H. H. *et al.* O-SNAP: A comprehensive pipeline for spatial profiling of chromatin architecture. *bioRxiv* 2025.07.18.665612 (2025) doi:10.1101/2025.07.18.665612.

22. Dhankhar, M. *et al.* Revealing the biophysics of lamina-associated domain formation by integrating theoretical modeling and high-resolution imaging. *Nat. Commun.* **16**, 7909 (2025).

23. Ahanger, S. H. *et al.* Distinct nuclear compartment-associated genome architecture in the developing mammalian brain. *Nat. Neurosci.* **24**, 1235–1242 (2021).

24. Gholamalamdari, O. *et al.* Major nuclear locales define nuclear genome organization and function beyond A and B compartments. *eLife* **13**, RP99116 (2025).

25. Su, J.-H., Zheng, P., Kinrot, S. S., Bintu, B. & Zhuang, X. Genome-Scale Imaging of the 3D Organization and Transcriptional Activity of Chromatin. *Cell* **182**, 1641-1659.e26 (2020).

26. Meuleman, W. *et al.* Constitutive nuclear lamina–genome interactions are highly conserved and associated with A/T-rich sequence. *Genome Res.* **23**, 270–280 (2013).

27. Wang, Y. *et al.* SPIN reveals genome-wide landscape of nuclear compartmentalization. *Genome Biol.* **22**, 36 (2021).

28. Siegenfeld, A. P. *et al.* Polycomb-lamina antagonism partitions heterochromatin at the nuclear periphery. *Nat. Commun.* **13**, 4199 (2022).

29. Liu, Y. *et al.* Systematic inference and comparison of multi-scale chromatin sub-compartments connects spatial organization to cell phenotypes. *Nat. Commun.* **12**, 2439 (2021).

30. Luo, Y. *et al.* New developments on the Encyclopedia of DNA Elements (ENCODE) data portal. *Nucleic Acids Res.* **48**, D882–D889 (2019).

31. Alexander, K. A. *et al.* p53 mediates target gene association with nuclear speckles for amplified RNA expression. *Mol. Cell* **81**, 1666-1681.e6 (2021).

32. Alexander, K. A. *et al.* Nuclear speckles regulate functional programs in cancer. *Nat. Cell Biol.* **27**, 322–335 (2025).

33. Kim, J., Venkata, N. C., Gonzalez, G. A. H., Khanna, N. & Belmont, A. S. Gene expression amplification by nuclear speckle association. *J. Cell Biol.* **219**, e201904046 (2019).

34. Stovall, D. B., Cao, P. & Sui, G. SOX7: from a developmental regulator to an emerging tumor suppressor. *Histol. Histopathol.* **29**, 439–45 (2013).

35. Zheng, W. *et al.* The role of Six1 in mammalian auditory system development. *Dev. (Camb., Engl.)* **130**, 3989–4000 (2003).

36. Solovei, I. *et al.* LBR and Lamin A/C Sequentially Tether Peripheral Heterochromatin and Inversely Regulate Differentiation. *Cell* **152**, 584–598 (2013).

37. Wong, X. *et al.* Mapping the micro-proteome of the nuclear lamina and lamina-associated domains. *Life Sci. Alliance* **4**, e202000774 (2021).

38. Dion, W. *et al.* SON-dependent nuclear speckle rehabilitation alleviates proteinopathies. *Nat. Commun.* **16**, 7065 (2025).

39. Kind, J. *et al.* Genome-wide Maps of Nuclear Lamina Interactions in Single Human Cells. *Cell* **163**, 134–147 (2015).

40. Muralikrishna, Bh. *et al.* Immunolocalization of detergent-susceptible nucleoplasmic lamin A/C foci by a novel monoclonal antibody. *J. Cell. Biochem.* **91**, 730–739 (2004).

41. Ikegami, K., Secchia, S., Almakki, O., Lieb, J. D. & Moskowitz, I. P. Phosphorylated Lamin A/C in the Nuclear Interior Binds Active Enhancers Associated with Abnormal Transcription in Progeria. *Dev. Cell* **52**, 699-713.e11 (2020).

42. Otterstrom, J. *et al.* Super-resolution microscopy reveals how histone tail acetylation affects DNA compaction within nucleosomes in vivo. *Nucleic Acids Res.* **47**, 8470–8484 (2019).

43. Nguyen, S. C. & Joyce, E. F. Programmable Chromosome Painting with Oligopaints. *Methods Mol. Biol. (Clifton, NJ)* **2038**, 167–180 (2019).

44. Petrovic, J. *et al.* Oncogenic Notch Promotes Long-Range Regulatory Interactions within Hyperconnected 3D Cliques. *Mol. Cell* **73**, 1174-1190.e12 (2019).

45. Stirling, D. R. *et al.* CellProfiler 4: improvements in speed, utility and usability. *BMC Bioinform.* **22**, 433 (2021).

46. Levet, F. *et al.* SR-Tesseler: a method to segment and quantify localization-based super-resolution microscopy data. *Nat. Methods* **12**, 1065–1071 (2015).

47. Xu, S., Grullon, S., Ge, K. & Peng, W. Spatial clustering for identification of ChIP-enriched regions (SICER) to map regions of histone methylation patterns in embryonic stem cells. *Methods Mol. Biol. (Clifton, NJ)* **1150**, 97–111 (2014).

Acknowledgments

We thank Dr. Brian Liau and Dr. Shelby Roseman for generously providing the SON/SRRM2 double-dTAG K562 cell line, and Dr. Andrew Belmont and Dr. Bas van Steensel for generously providing the LMNA and LBR knockout K562 cells.

Material and Methods

This research complies with all relevant ethical regulations for studies involving cultured human cell lines by University of Pennsylvania.

Experimental methods

Cell culture

K562 derivatives—SON/SRRM2 FKBP12 double knock-in, LMNA knockout (LMNA−/−), and LBR knockout (LBR−/−)—were maintained in RPMI-1640 containing 2 mM L-glutamine (Invitrogen, 11875085), 10% fetal bovine serum (FBS), and 1% penicillin–streptomycin at 37 °C with 5% CO_2. Lymphoblastoid cell lines (LCLs) were cultured in RPMI-1640 supplemented with 10% FBS and 1% penicillin–streptomycin under identical conditions.

For acute speckle disruption, cells were treated with 500 nM dTAG v1 (Tocris 6914) for 24 h unless otherwise indicated; matched DMSO (Sigma D8418) vehicle controls were included. For pharmacologic speckle activation, pyrvinium pamoate (PP, Sigma P0027) was applied at 100 nM for 24 h unless noted.

All experiments used independently grown and treated biological replicates. Cell line identity and genotype were confirmed by Sanger sequencing and/or immunoblotting against the relevant tagged proteins. Cultures were routinely screened and found negative for mycoplasma contamination at least every six months.

Western blotting

Samples were lysed with RIPA buffer (150nM NaCl, 1% IGEPAL, 0.5% sodium deoxycholate, 0.1% SDS and 50mM Tris pH7.4). Protein concentration was determined by bicinchoninic acid assay (BCA) protein assay (#23227, Life Technologies). Samples were separated using precast 4-12% Bis-Tris polyacrylamide gels (ThermoFisher Scientific, NP0321BOX) in the presence of SDS. Proteins were transferred to nitrocellulose membrane, blocked with 5% milk TBST and probed with designated primary antibodies overnight at 4°C. Following TBST wash steps, membranes were incubated in secondary goat anti rabbit antibody (1:10000, Bio-Rad, 1706515) for one hour, washed with TBST, and detected using using Thermo Scientific SuperSignal West Pico PLUS Chemiluminescent Substrate (ThermoFisher Scientific, 34577). Signal quantification was performed using ImageJ software.

Immunofluorescence and antibodies

Cells were washed twice with PBS and fixed with Paraformaldehyde solution 4% in PBS (Santa Cruz Biotechnology, CAS 30525-89-4) for 10 minutes at room temperature, washed again with PBS (Corning, 21-031-CV) then permeated with 0.1% PBS Triton X-100 for 15 minutes. Cells were incubated overnight in primary antibodies targeting GFP to stain GFP labelled SON (abcam, ab121759) or SRRM2 (Sigma-Aldrich, S4045) diluted 1:200 in PBS at 4C. Secondary antibody conjugated with Goat anti-Rabbit IgG Alexa Fluor™ 488 (ThermoFisher Scientific, A-11008) and Goat anti-Mouse IgG

Alexa Fluor™ 647 (ThermoFisher Scientific, A-21235) were diluted 1:200 in PBS and used respectively. After 1 hour incubation at room temperature, samples were washed and incubated in 1:10000 DAPI (Invitrogen, D1306, 5 mg/mL) for 5min. Imaging was performed with Nikon Eclipse Ti2 widefield microscope. Cells were imaged at focal plane with a 40x objective, and a deep depletion CCD camera cooled to between -70 and -80C.

Stochastic Optical Reconstruction Microscopy (STORM) imaging

Immunofluorescence was performed as described previously and in[42] , using a 1:50 dilution of anti-H3 primary antibody (Active Motif, 39763) and a 1:50 dilution of Alexa Fluor™ 647–conjugated secondary antibody (Thermo Fisher Scientific, A-21235) in PBS. STORM imaging was performed as described in the literature[21] . Briefly, images were acquired on an ONI Nanoimager (Oxford Nanoimaging) controlled by NimOS software (v1.19.4) using the 640-nm laser (exciting AF647). Cells were imaged in buffer containing 0.1 M cysteamine (MEA; 77 mg/mL stock; Sigma-Aldrich, 30070-10G prepared in 360 mM HCl; Fisher, A508-P500), 5% (w/v) glucose (Alfa Aesar, A16828), and a 1% GLOX solution. The GLOX solution was prepared by dissolving 14 mg glucose oxidase (Sigma-Aldrich, G2133) in 50 µL catalase (20 mg/mL; Roche, 106810) and bringing to 200 µL with 10 mM Tris (pH 8.0; Invitrogen, 15568025) containing 50 mM NaCl (Fisher, S217-500). Imaging buffer was replaced every 90 min. Acquisition settings were 15-ms exposure for 30,000 frames at 30 °C with constant high-intensity illumination at 647-nm excitation.

Oligopaint DNA-FISH

Sample slides were fixed with 4% PFA in PBS for 10 minutes at room temperature, washed with PBS and permeabilized with 0.5% Triton in PBS for 15 minutes. Subsequently, DNA-FISH was performed as described[43]. Oligopaint DNA-FISH probes to target genes were designed across a 50kb region centered on the transcription start site as described[44]. Imaging was performed with Nikon Eclipse Ti2 widefield microscope. Cells were imaged at focal plane with a 40x objective.

CUT&RUN sequencing

CUT&RUN was performed as described previously with minor modification[23]. For each condition, nuclei from ~6×10^5 cells were isolated in nuclear isolation buffer (10 mM HEPES-KOH pH 7.9, 10 mM KCl, 0.1% NP-40, 0.5 mM spermidine, 1× Halt protease inhibitor cocktail) and bound to concanavalin A–coated magnetic beads (BioMag Plus) pre-equilibrated in binding buffer (20 mM HEPES-KOH pH 7.9, 10 mM KCl, 1 mM $CaCl_2$, 1 mM $MnCl_2$). After bead binding, samples were split for antibody incubations; binding buffer was replaced with primary antibody diluted 1:100 in blocking buffer (20 mM HEPES-KOH pH 7.5, 150 mM NaCl, 0.1% BSA, 0.5 mM spermidine, 1× Halt protease inhibitor cocktail, 2 mM EDTA). Normal IgG (Millipore 06-371) was included as a negative control. Bead–nuclei were rotated overnight at 4 °C, washed in washing buffer (20 mM HEPES-KOH pH 7.5, 150 mM NaCl, 0.1% BSA, 0.5 mM spermidine, 1× Halt protease inhibitor cocktail), and incubated with pA-MNase on ice. Digestion was initiated by addition of $CaCl_2$ and carried out for 30 min on a pre-chilled metal block on ice. Reactions were stopped by adding STOP buffer (200 mM NaCl, 20 mM EDTA, 4 mM EGTA, 50 µg/mL RNase A, 40 µg/mL glycogen) with gentle vortexing, followed by fragment release at 37 °C for 10 min. Supernatants were collected, treated with Proteinase K at 70 °C for 10 min, and DNA was purified by phenol:chloroform:isoamyl alcohol extraction. Libraries were prepared from released DNA using the NEBNext Ultra II DNA Library Prep Kit for Illumina, size

profiles were assessed on an Agilent TapeStation, and concentrations quantified with the NEBNext Library Quant Kit (E7630, NEB). Libraries were sequenced on an Illumina NextSeq 1000 using NextSeq™ 1000/2000 P2 XLEAP-SBS™ Reagent Kit with 61bp per read.

Polyadenylated RNA-seq

Cells were lysed in TRIzol (15596018, Thermo Fisher Scientific) and snap frozen. RNA was then isolated using chloroform extraction, followed by Zymo Direct-zol RNA Miniprep Kits (Zymo Research, R2050), including DNA digestion with DNase. Poly(A)+ RNA was further isolated using double selection with poly-dT beads (E7490, NEB). RNA-seq libraries were prepared using the NEBNext Ultra II Directional Library Prep Kit for Illumina (E7760, NEB). The size of the libraries was determined using a Bioanalyzer, and their concentration was determined using the NEBNext Lib Quant Kit (E7630, NEB). Libraries were sequenced on an Illumina NextSeq 1000 using NextSeq™ 1000/2000 P2 XLEAP-SBS™ Reagent Kit with 61bp per read.

Data processing and analysis

Statistics & Reproducibility

Details of the statistical tests are documented in the sections below for each analysis. For all replicate experiments in this study, cells were grown and treated separately as biological replicates. No statistical methods were used to pre-determine sample sizes but our sample sizes are similar to those reported in previous publications [6,31]. For all image-based statistics, two-sided Wilcoxon test was performed, and no assumption of data distribution was made.

Immunofluorescence (IF) data processing and analysis

All IF images were taken at the focal plane with the autofocus function of Nikon NIS software (5.30.04) on a Nikon Eclipse Ti2 widefield microscope, except for the STORM imaging in Figure 1B and 6B. Subsequent image processing was performed with CellProfiler[45] (version 4.2.1, https://cellprofiler.org/) to identify nuclear speckle and measure various size, shape and intensity parameters. Pipeline and notes are available on Github: https://github.com/Chalietia/CellProfiler/.

DNA-FISH processing and analysis

Images were preprocessed (flat-field correction and background subtraction) and analyzed in CellProfiler (version 4.2.1) with custom pipelines available at https://github.com/Chalietia/CellProfiler. Nuclei were segmented from DAPI using adaptive thresholding and size/shape filters to remove debris and touching clumps. DNA-FISH foci were detected per nucleus using a Laplacian-of-Gaussian spot detector with intensity and size thresholds chosen from control images; nuclei harboring >4 foci (indicative of over-segmentation or multiplets) were excluded a priori. Distances were measured in pixels and converted to physical units using the system pixel size (0.13 µm/pixel). Distance distributions were summarized as medians with interquartile ranges and compared across conditions using two-sided Mann–Whitney–Wilcoxon tests; where multiple comparisons were performed, p-values were adjusted by the Benjamini–Hochberg method.

STORM imaging analysis

Localizations at the nucleus were manually segmented from the field of view. The local compaction maps of the STORM image data were generated using Voronoi tessellation as previously described[46] , where each Voronoi cell is pseudo-colored based on its respective area. In addition to the maps, O-SNAP (Objective Single-Molecule Nuclear Architecture Profiler; https://github.com/LakGroup/O-SNAP) was performed on the H3 localization data as described in the literature[21]. Briefly, the pipeline extracts 144 features from single molecule localization data. The features describe properties such as nucleus morphology as well as global and local organization of the H3 signal. O-SNAP then conducts parallel, orthogonal analyses to perform feature exploration. A volcano analysis identifies features that change most dramatically between experimental groups based on fold change and statistical significance using Welch's t-test with the Benjamini-Hochberg method for multiple test correction. Here, O-SNAP highlights the modeled LAD thickness; the process for generating these modeled LAD segments is originally described in literature[22].

CUT&RUN data processing

Sequencing reads were aligned to the human reference genome GRCh38/hg38 using Bowtie2 v2.3.4.1 with the following parameters: --very-sensitive-local --no-mixed --no-discordant -I 10 -X 1000 -x hg38. Alignments were filtered with samtools v1.1 (view -q 5), sorted and indexed, and PCR duplicates were removed with Picard v2.26 (MarkDuplicates, REMOVE_DUPLICATES=true). Reads mapping to ENCODE hg38 blacklist regions were excluded from all downstream analyses (hg38 blacklist v2). Signal tracks (bigWig/bedGraph) were generated with deepTools (bamCompare) using -bs 5000 --smoothLength 15000 --effectiveGenomeSize 2913022398 --exactScaling --normalizeUsing RPKM --scaleFactorsMethod None -bl <hg38_blacklist.bed>, comparing each target to its matched IgG control.

CUT&RUN/DamID differential analysis and SWING domain definition

Differential analysis followed a published sliding-window framework[31] (step-by-step: https://github.com/katealexander/TSAseq-Alexander2020/tree/master/genomicBins_DiffBind) with minor modifications. Briefly, PCR-deduplicated BAMs (targets with matched inputs/controls) were quantified over 50-kb windows tiled across hg38 at a 5-kb step (1/10 window) using DiffBind v3.12.0 (https://bioconductor.org/packages/release/bioc/html/DiffBind.html) with input subtraction enabled. Custom blacklist regions (generated as described above) and ENCODE hg38 blacklist were supplied to DiffBind via dba.blacklist(). Library-size normalization used DBA_NORM_RLE. Windows showing significant SON signal change (FDR < 0.01, Benjamini–Hochberg) were split by direction and merged into contiguous intervals with BEDTools (merge) to yield differential domains. For SWING domain calls, differential regions exhibiting a significant increase in Lamin B1 signal (FDR < 0.01) in K562 dTAG-treated versus control, or in patient (P276) versus healthy donor (S1), were designated as SWING domains. Genes were assigned to domains by intersecting domain intervals with transcription start sites; genes whose TSS fell within a differential domain were extracted using a Python script adapted from getGenesWithin.py in the referenced workflow.

LAD and SPAD calling

Broad domains were called with SICER (v1.1) [47] on hg38 using the following assay-matched controls: matched IgG for CUT&RUN, no-primary control for TSA-seq, and no-Dam (Dam-only) control for

DamID: sicer -t <signal.bam> -c <control.bam> -s hg38 -fdr 0.1 -w 2000 -g 20000. For SPADs, <signal> was SON CUT&RUN or SON TSA-seq libraries; for LADs, <signal> was Lamin B1 CUT&RUN or Lamin B1 DamID, as indicated. Resulting BED files were sorted and filtered to remove ENCODE hg38 blacklist regions. Consensus domains for each condition were defined by strict replication: domains present in all biological replicates were intersected with bedtools (intersect, optionally followed by merge to consolidate adjacent fragments), and the shared overlap was taken as the final set for downstream analyses. When overlap with SWING domain, SWING domain takes priority and corresponding overlapping region is removed by bedtools subtract. When LAD/SPAD domains overlapped SWING domains, SWING regions were given precedence. Overlapping bases were removed from the LAD/SPAD sets using bedtools subtract followed by sorting.

Gene ontology (GO) analysis

Gene sets comprising (i) genes of which TSSs reside within SWING domains and/or (ii) genes with significant differential expression by RNA-seq (as described in Results) were analyzed with STRING (https://string-db.org/; organism: Homo sapiens) using default enrichment settings. GO Biological Process terms were tested with STRING's built-in over-representation analysis and Benjamini–Hochberg multiple-testing correction; terms with FDR < 0.05 were considered significant. To reduce redundancy, significant terms were clustered by similarity at a threshold of 0.8, and representative terms were reported. Unless fewer were available, the first 10 significant (non-redundant) terms are shown. Input identifiers were supplied as official gene symbols, and background was set to the STRING genome-wide reference.

RNA-seq processing and differential analysis

Reads were aligned to the human reference genome GRCh38/hg38 with STAR v2.7.1a (https://github.com/alexdobin/STAR) using:--outFilterType BySJout --outFilterMultimapNmax 20 --alignSJoverhangMin 8 --alignSJDBoverhangMin 1 --outFilterMismatchNmax 999 --outFilterMismatchNoverReadLmax 0.04 --alignIntronMin 20 --alignIntronMax 1000000.Alignments were quantified to RefSeq gene models (GRCh38) using htseq-count (v0.11.1) in union mode (--type exon --idattr gene_id -s no). Gene-level normalization and differential expression were performed with DESeq2 (v1.40.2) using default settings (size-factor normalization; Wald test; Benjamini–Hochberg adjustment). Unless otherwise indicated, genes with FDR < 0.05 and absolute log2 fold change >1 were considered differentially expressed. Statistical differences between log2 fold changes of predefined gene groups were assessed using two-sided Mann–Whitney–Wilcoxon tests; where multiple comparisons were made, p-values were adjusted by the Benjamini–Hochberg method.

Figure legends

Figure 1. Disruption of nuclear speckles increases lamina association of specific genomic domains.

(A) Western blot of FKBP12-tagged core speckle proteins SON and SRRM2 after the indicated durations of dTAG treatment; GAPDH serves as a loading control.

(B) Representative STORM image from K562 SON/SRRM2 double knock-in cells with or without dTag treatment for 24hr; the color scale encodes log10 Voronoi polygon area.

(C) Quantification of nuclear area (left) and LAD thickness (right) from STORM datasets. Violin plots show the distribution (kernel density) with embedded box plots (median, interquartile range [IQR]; whiskers, 1.5× IQR). *P* values were computed by two-sided Welch's *t*-tests with Benjamini–Hochberg correction for multiple comparisons.

(D–E) Representative genome browser tracks (three biological replicates per condition) for DMSO and dTAG-treated samples. Red arrows mark regions with increased lamina association upon dTAG treatment. Bottom tracks indicate domain calls: LAD (red), SWING (purple), and SPAD (blue). A zoomed-out view of the light-blue highlighted region is shown at right.

(F) Metagene profiles and heatmaps of Lamin B1 CUT&RUN signal across all called LADs, SWING domains, and SPADs in DMSO versus dTAG-treated K562 cells.

(G–H) (Top) DNA-FISH images using probes targeting a SPAD locus (cyan) and a SWING locus (magenta) in DMSO- or dTAG-treated cells. (Bottom) Corresponding Lamin B1 CUT&RUN browser tracks and quantification of 3D distances from FISH signals to the nuclear periphery. Box plots as in (C); *P* values by two-sided Mann–Whitney *U* test. Each dot represents one FISH foci.

Figure 2. SWING domains exhibit intermediate properties.

(A–B) Quantification of speckle association (SON TSA-seq signal; A) and nuclear lamina association (Lamin B1 DamID signal; B) across LADs, SWING domains, and SPADs in K562 cells. Violin plots show distributions with embedded box plots (median, IQR; whiskers 1.5× IQR) where applicable. *P* values are from two-sided Mann–Whitney U tests.

(C) 2D density plot showing Lamin B1 level (x-axis) versus SON–TSA-seq signal (y-axis) for LADs, SWING domains, and SPADs. 2D density plots display kernel density estimates.

(D–E) Multiplex DNA-FISH (MERFISH) in IMR90 cells quantifying foci-to-speckle distance (D) and foci-to-lamina distance (E) for loci in LADs, SWING domains, and SPADs.

(F) 2D density plot of MERFISH measurements for loci classified as LAD, SWING, or SPAD.

(G) Example browser view of Lamin B1 DamID signal across four cell lines; bottom red track shows the per-bin standard deviation across cell lines. BED tracks indicate domain calls: LAD (red), SWING (purple), SPAD (blue).

(H) Variability of Lamin B1 signal across four cell lines, summarized as standard deviation within LADs, SWING domains, and SPADs.

(I) Proportions of low-, mid-, and high-variability regions (bottom, middle, and top tertiles by standard deviation) within LAD, SWING, and SPAD categories.

(J) Representative view in K562 cells showing Lamin B1 CUT&RUN signal, corresponding SWING domain calls, and Hi-C subcompartment annotations.

(K) Distribution (% of bases) of A1, A2, B1, and B2 subcompartments genome-wide (All) and within LADs, SWING domains, and SPADs in K562 cells.

(L) Subcompartment enrichment (log2 odds ratio) for A1, A2, B1, and B2 within All, LAD, SWING, and SPAD regions in K562 cells.

Figure 3. SWING domains become more heterochromatin-like upon speckle disruption.

(A) Percentile distributions of designated histone-modification ChIP–seq signals across LADs, SWING domains, and SPADs.

(B) Example browser view of H3K27me3 and H3K9me3 CUT&RUN signal in control K562 cells. BED tracks indicate domain calls: LAD (red), SWING (purple), SPAD (blue).

(C) Representative IF images for H3K9me3 and H3K27me3 in K562 cells with or without 24 h dTAG treatment.

(D) Quantification of distances from the nuclear periphery for regions classified as H3K9me3-only, H3K9me3+H3K27me3, or H3K27me3-only in K562 cells with or without 24 h dTAG treatment. Violin plots display the distribution with embedded box plots (median, interquartile range [IQR]; whiskers, 1.5× IQR). P values by two-sided Mann–Whitney U tests.

(E) Example browser view of H3K27me3 and H3K9me3 CUT&RUN signal in K562 cells with or without 24 h dTAG treatment; blue arrows indicate regions with reduced signal and red arrows indicate regions with increased signal.

(F–G) Metagene profiles and heatmaps of H3K27me3 (F) and H3K9me3 (G) CUT&RUN signal across all called LADs, SWING, and SPADs in DMSO versus dTAG-treated K562 cells. Metagene lines show mean normalized CUT&RUN signal with shaded 95% CI; heatmaps display z-scored signal per region, centered at region midpoints and ordered by mean signal.

(H) Percentages of (left) all differential regions and up-regulated H3K9me3 regions and (right) all differential regions and down-regulated H3K27me3 regions within LADs, SWING domains, and SPADs. Bars show category proportions.

(I) Enrichment of H3K9me3-upregulated regions and H3K27me3-downregulated regions across LADs, SWING, and SPADs, reported as log2 (observed/expected).

Figure 4. Nuclear speckle disruption leads to down-regulation of SWING genes.

(A) Comparison of significantly differentially expressed genes (FDR < 0.05 and |log2 fold change| > 1) between dTAG 24 h and DMSO in K562 cells, grouped by localization (SPAD vs SWING). Box plots show median and IQR; whiskers, 1.5× IQR. P values by two-sided Mann–Whitney U tests.

(B) Percentile distributions showing the proportions of significantly down-regulated (blue) and up-regulated (red) genes within SPAD or SWING.

(C) Distributions of log2 fold change for expression-matched SPAD versus SWING genes (no FDR or fold-change cutoff). Lines show mean with shaded 95% CI.

(D) RNA-seq heatmap of all significantly differentially expressed genes in SWING and SPAD with hierarchical clustering. The y-axis lists individual genes; SPAD genes are labeled blue and SWING genes purple. Values are z-scores of normalized RNA-seq counts.

(E) Volcano plot of dTAG 24 h versus DMSO in K562. Points are colored by domain localization (SPAD, blue; SWING, purple). “Sig” denotes significantly differentially expressed genes (FDR < 0.05 and |log2 fold change| > 1); “NS” denotes not significant.

(F) Example browser view showing Lamin B1 CUT&RUN tracks and normalized RNA-seq counts for genes within SPAD (FAAH, POLH) and within SWING (LINC02794, CYP39A1). The “domain” BED track indicates calls: LAD (red), SWING (purple), SPAD (blue).

(G) HOMER motif-enrichment results for SWING domains; entries highlighted in red denote development-related transcription factors.

(H) Gene Ontology Biological Process enrichment for significantly decreased SWING genes (FDR < 0.05 and log2 fold change < −1) in dTAG 24 h versus DMSO K562 cells; development-related terms are highlighted.

Figure 5. SWING domains relocate away from the lamina upon LMNA disruption.

(A) Representative genome browser view of Lamin B1 DamID signal in WT, LMNA KO, and LBR KO K562 cells. Blue arrows mark regions with decreased lamina association; red arrows mark regions with increased lamina association in the indicated genotype. Bottom tracks indicate domain calls: LAD (red), SWING (purple), SPAD (blue). A zoomed-out view of the light-blue highlighted region is shown at right.

(B) Metagene profiles and heatmaps of Lamin B1 DamID signal across all called LADs, SWING domains, and SPADs in WT, LMNA KO, and LBR KO K562 cells.

(C) Heatmap of z-score–normalized Lamin B1 DamID signal in WT, LMNA KO, and LBR KO K562 cells with hierarchical clustering, grouped by domain category (LAD, red; SWING, purple; SPAD, blue).

(D) Proportions (%) of significantly increased or decreased Lamin B1–associated regions in LBR KO (left) and LMNA KO (right), colored by domain category (LAD, red; SWING, purple; SPAD, blue). Bars show category proportions.

(E) Comparison of log2 fold change in gene expression across K562 conditions—dTAG-mediated speckle disruption, LMNA KO, and LBR KO—for genes that show significantly decreased Lamin B1 association (FDR < 0.01) in LMNA KO cells. Box plots show median and IQR; whiskers, 1.5× IQR.

(F) Example browser view showing Lamin B1 DamID tracks and normalized RNA-seq counts for indicated genes; light-blue shading highlights gene bodies.

Figure 6. Speckle activation by drug treatment reduces lamina tethering.

(A) Left: representative IF images in K562 cells under the indicated treatments and antibodies. Right: quantification of speckle area and speckle count per nucleus. Violin plots show distributions with embedded box plots (median, IQR; whiskers, 1.5× IQR). P values by two-sided Mann–Whitney U tests.

(B) Representative STORM image from K562 SON/SRRM2 double knock-in cells with or without PP (pyrvinium pamoate) treatment; the color scale encodes log10 Voronoi polygon area.

(C) Quantification of nuclear area (left) and LAD thickness (right) from STORM datasets. Violin plots as in (A). P values by two-sided Welch's t-tests with Benjamini–Hochberg correction for multiple comparisons.

(D) Sanger sequencing of the SON locus in a healthy control and patient 276; red arrow indicates the heterozygous point mutation.

(E) Representative IF for SRRM2 in LCLs from a healthy donor and patient 276 (P276), with or without 100 nM PP.

(F–G) Quantification of speckle area (F) and speckle count (G) per nucleus for IF in the indicated cell lines and conditions. Violin plots as in (A); P values by two-sided Mann–Whitney U tests.

(H) Representative genome browser view of Lamin B1 CUT&RUN signal in healthy donor (S1), patient 276 (P276), and P276 treated with 100 nM PP. Blue arrows mark regions with decreased lamina association; red arrows mark regions with increased lamina association in the indicated sample. Bottom tracks indicate domain calls: LAD (red), SWING (purple), SPAD (blue). A zoomed-out view of the light-blue highlighted region is shown at right.

(I) Metagene profiles and heatmaps of Lamin B1 CUT&RUN signal across all called LADs, SWING domains, and SPADs, in S1, P276, and P276 with 100 nM PP. Metagene lines show mean normalized signal; heatmaps display z-scored signal per region, centered at region midpoints and ordered by mean signal.

(J) Overlap between SWING domains identified in K562 and in patient 276. P value by hypergeometric test using the hg38 mappable genome as background.

(K) Overlap between SWING domains and regions showing significant rescue of aberrant Lamin B1 under PP treatment in patient 276. P value by hypergeometric test using the hg38 mappable genome as background.

(L) Percentile distribution of regions with significant Lamin B1 rescue under PP treatment in patient 276 across LAD and SWING domains.

(M) Heatmap of z-score–normalized Lamin B1 signal across all P276+PP versus P276 differential regions (FDR < 0.01) in the indicated samples, with hierarchical clustering.

Figure 7. Developmental pathway dysregulation in speckleopathy patient cells is mitigated by pyrvinium pamoate.

(A) Volcano plot of RNA-seq differential analysis between patient 276 (P276) and healthy donor (S1). Points are colored by domain localization (SPAD, blue; SWING, purple). "Sig" denotes significantly differentially expressed genes (FDR < 0.05 and |log2 fold change| > 1); "NS" denotes not significant. Axes: x, log2 fold change; y, −log10 FDR.

(B) Comparison of significantly differentially expressed genes (FDR < 0.05 and |log2 fold change| > 1) between P276 and S1, grouped by localization (SPAD vs SWING). Box plots show median and IQR; whiskers, 1.5× IQR. P values by two-sided Mann–Whitney U tests.

(C) Percentile distributions showing the proportions of significantly down-regulated (blue) and up-regulated (red) genes within SPAD or SWING.

(D) RNA-seq heatmap of all significantly differentially expressed genes in SWING and SPAD with hierarchical clustering between P276 and S1. The y-axis lists individual genes; SPAD genes are labeled blue and SWING genes purple. Values are z-scores of normalized RNA-seq counts (per-gene z-scaling; distance = 1 − Pearson correlation; average linkage).

(E) Comparison of log2 fold change relative to S1 for genes that show Lamin B1 rescue under PP (100 nM) in P276 (untreated) versus P276+PP. Paired points are connected per gene; P values by two-sided Wilcoxon signed-rank test.

(F) RNA-seq heatmap of genes with Lamin B1 rescue under PP that are significantly affected by PP (FDR < 0.10); development-related genes are highlighted in red.

(G) Example browser view showing Lamin B1 CUT&RUN tracks and normalized RNA-seq counts for indicated genes; light-blue shading highlights gene bodies.

(H) Gene Ontology Biological Process enrichment for genes rescued by PP (RNA-seq: P276+PP vs P276, FDR < 0.10 and fold change > 0; Lamin B1 CUT&RUN: decreased Lamin B1 in P276+PP vs P276, FDR < 0.01). Development-related terms are highlighted.

(I) Schematic illustrating the model of joint regulation of SWING domains by nuclear speckles and nuclear lamina.

Supplementary Figure legends

Supplementary Figure 1.

(A) Representative images (Left) and quantification (Right) of IF-staining granularity and radial coefficient of variation for four nuclear speckle localized factors: SON, SRRM2, RBM25, and SF3A66, in K562 cells with or without dTAG treatment for 24 h. Violin plots show distributions with embedded box plots (median, IQR; whiskers, 1.5× IQR). P values by two-sided Mann–Whitney U tests.

(B) Western blot for H3 and SRRM2 in K562 cells with or without dTAG treatment; GAPDH serves as a loading control.

(C) STORM images of K562 SON/SRRM2 double knock-in cells with (top) or without (bottom) 24 h dTAG treatment; the color scale encodes log10 Voronoi polygon area.

Supplementary Figure 2.

(A) Representative genome browser tracks for three biological replicates of DMSO-treated K562 cells (left) and pairwise Pearson correlation among the three replicates (right).

(B) Representative genome browser tracks of Lamin B1 DamID and Lamin B1 CUT&RUN in K562 cells (left) and Pearson correlation between DamID and CUT&RUN signals (right).

(C) Representative IF images of Lamin B1 in K562 cells with or without 24 h dTAG treatment.

(D) Western blot for Lamin B1 in the indicated samples; GAPDH serves as a loading control.

Supplementary Figure 3.

(A) Volcano plot of RNA-seq differential expression in K562 (dTAG 24 h vs DMSO). Genes with FDR < 0.05 and |log2 fold change| > 1 are considered significant. Axes: x, log2 fold change; y, −log10 FDR.

(B) Comparison of expression levels for genes located in LAD, SWING, and SPAD in DMSO-treated K562 cells. Box plots show median and IQR; whiskers, 1.5× IQR.

(C) Gene Ontology Biological Process enrichment for all genes located in SWING domains identified in K562 cells; selected development-related terms are highlighted.

Supplementary Figure 4.

(A) Human Phenotype Ontology (HPO) terms annotated for patient 276.

(B) RNA-seq normalized counts for SON transcripts.

(C) Gene Ontology Biological Process enrichment for all genes located in SWING domains identified in patient 276.

(D) Volcano plot of RNA-seq differential expression comparing patient 276 and healthy donor (S1) LCLs. Genes with FDR < 0.05 and |log2 fold change| > 1 are considered significant. Axes: x, log2 fold change; y, −log10 FDR.

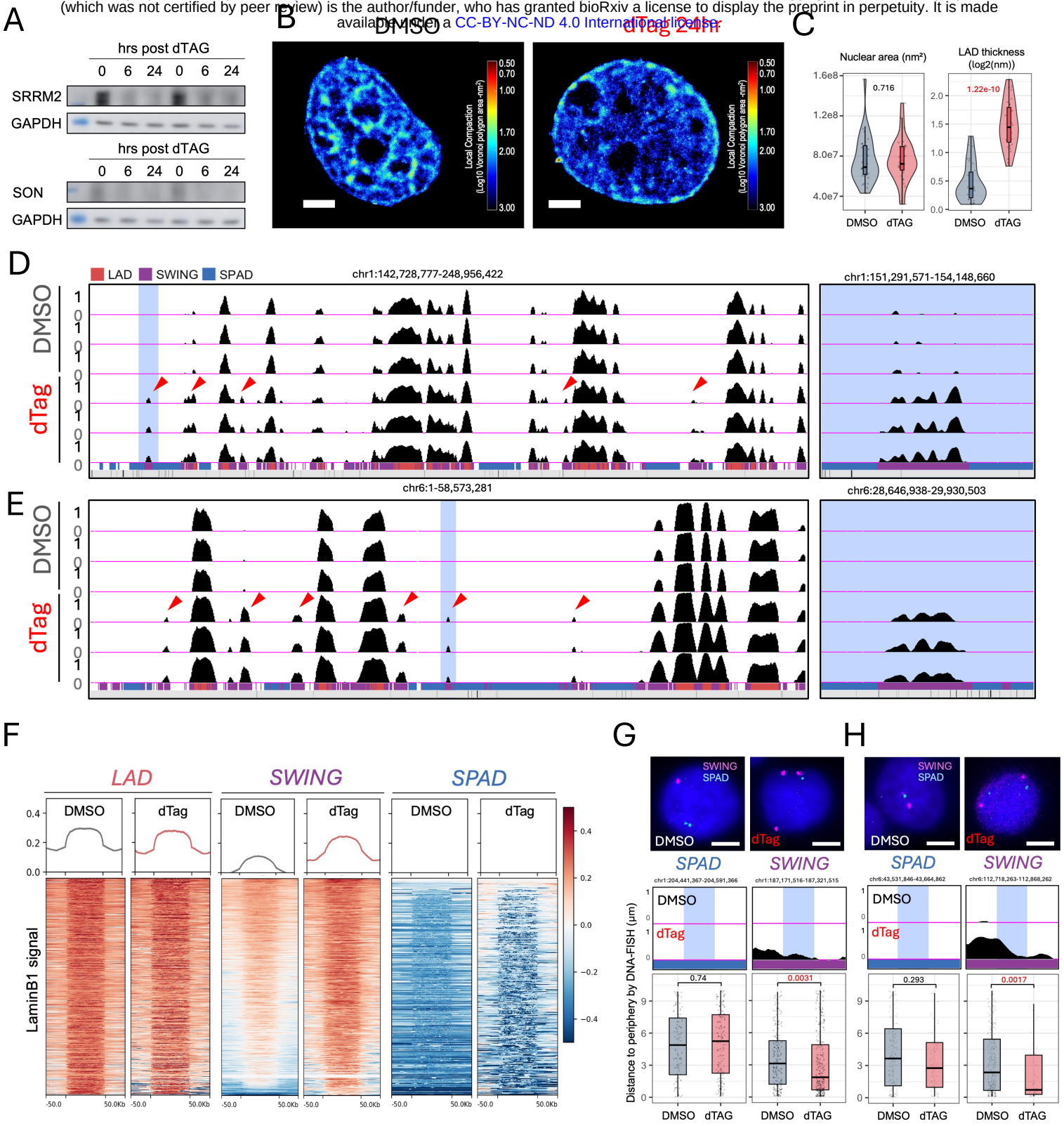

Figure1

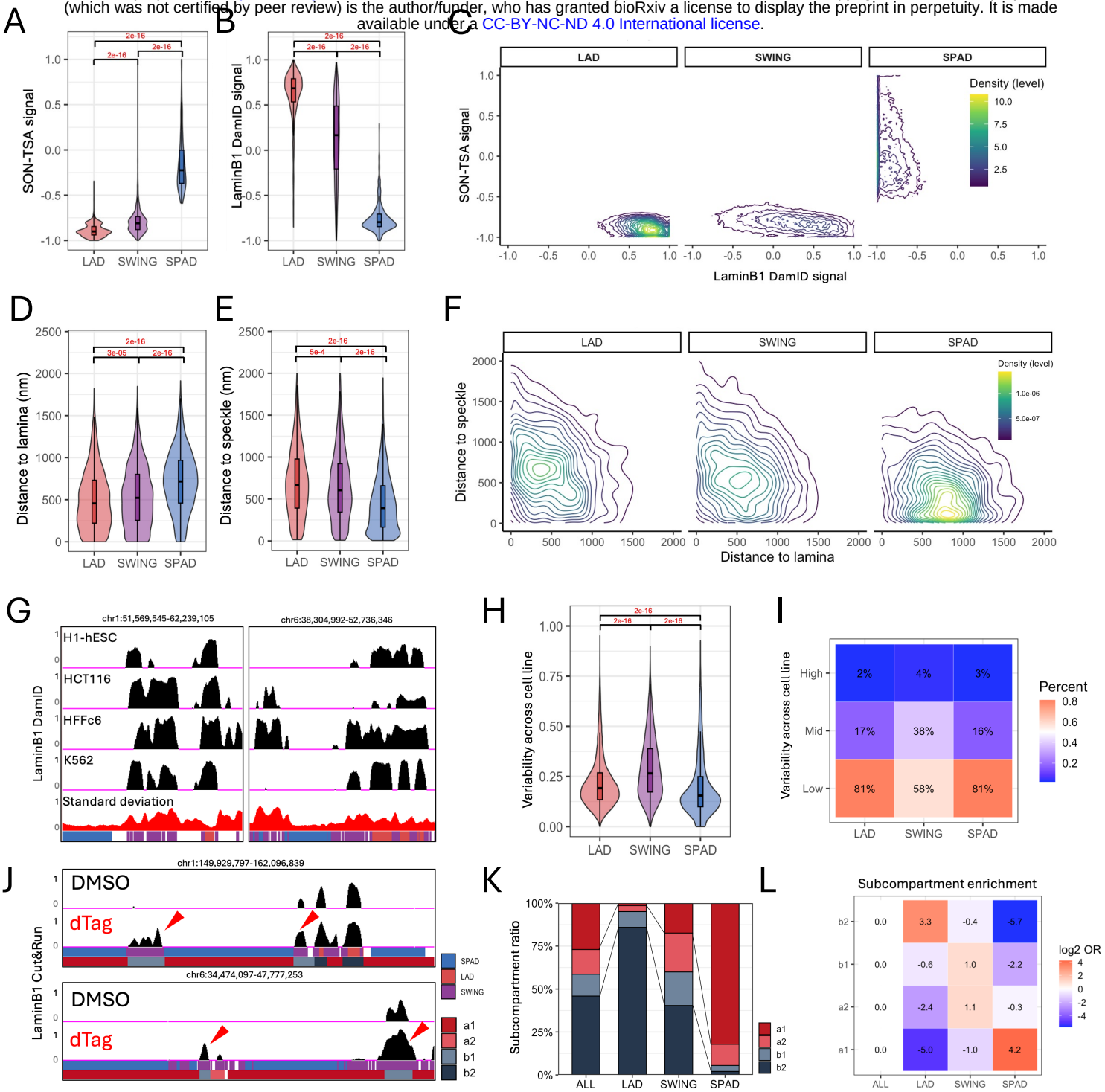

Figure2

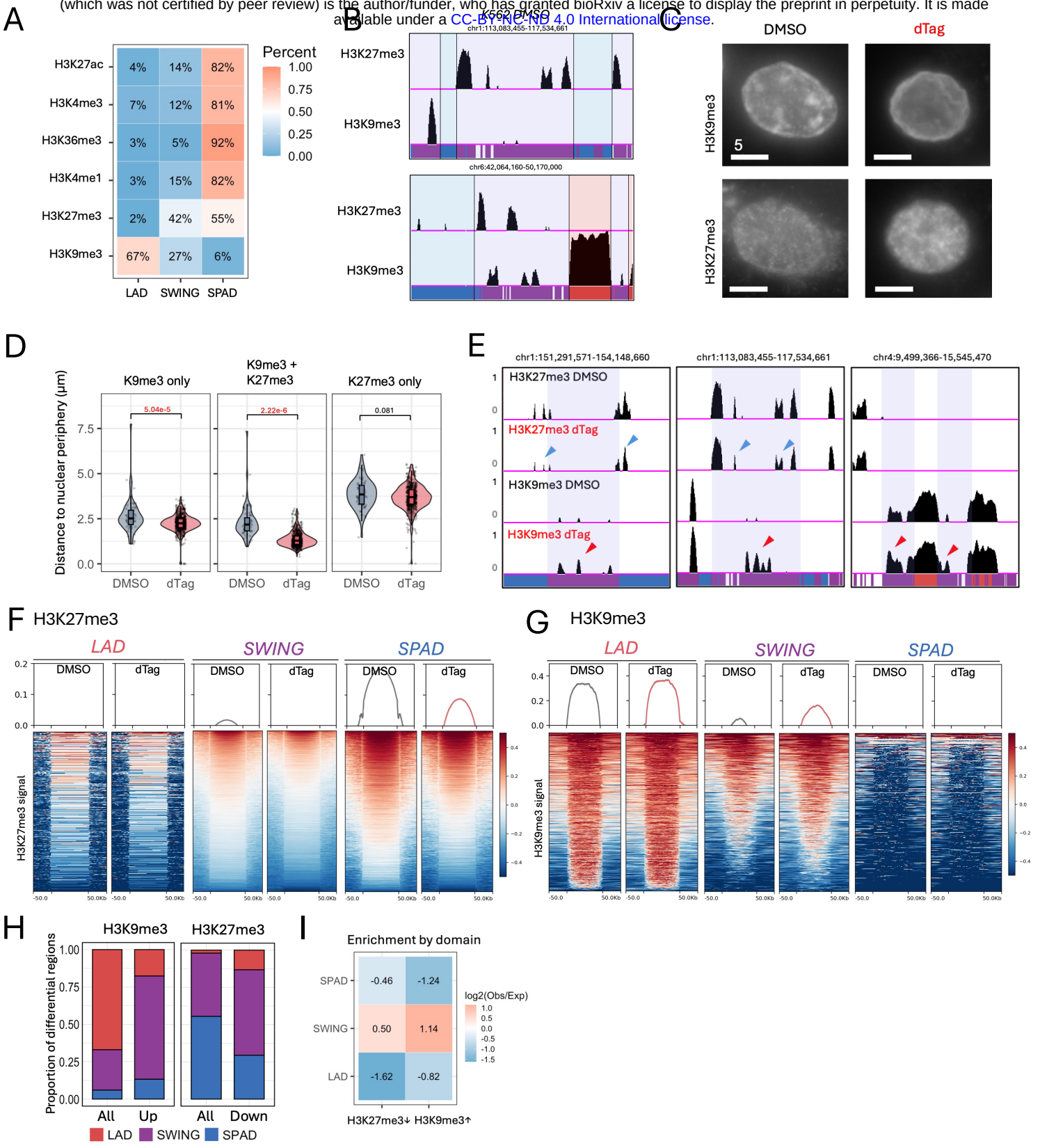

Figure3

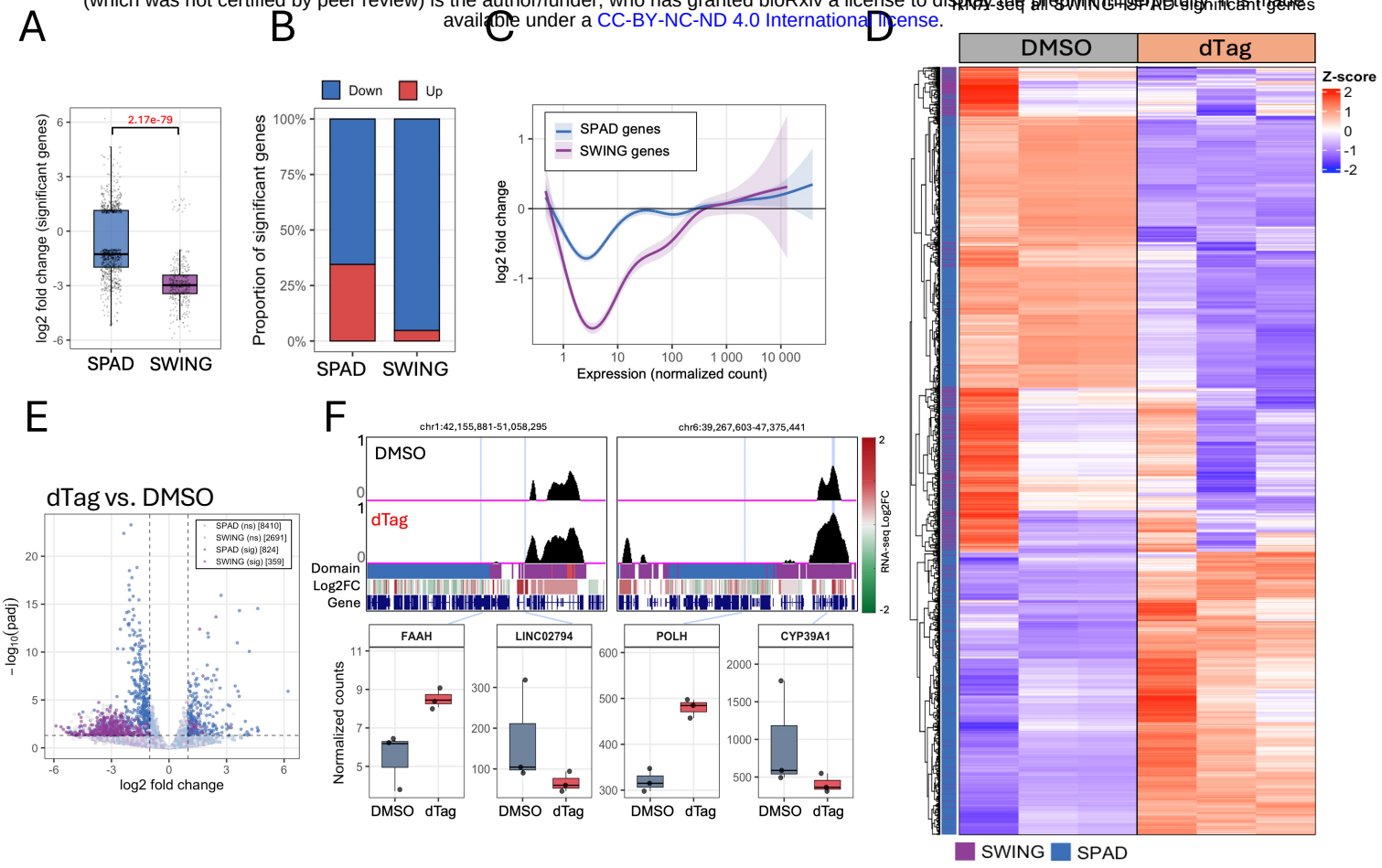

G

Enrichment	log10p	BestMatch	Motif
4300.00%	11.00	Sox7	
3900.00%	11.00	ZNF692	
2600.00%	12.00	Six1	
2400.00%	11.00	Lhx4	
2150.00%	10.00	ZNF263	
1866.67%	11.00	Erra	
1733.33%	10.00	ZNF652	
1525.00%	11.00	RUNX	
1380.00%	13.00	ZNF148	
1300.00%	7.00	SOX2	
1300.00%	9.00	Foxk1	

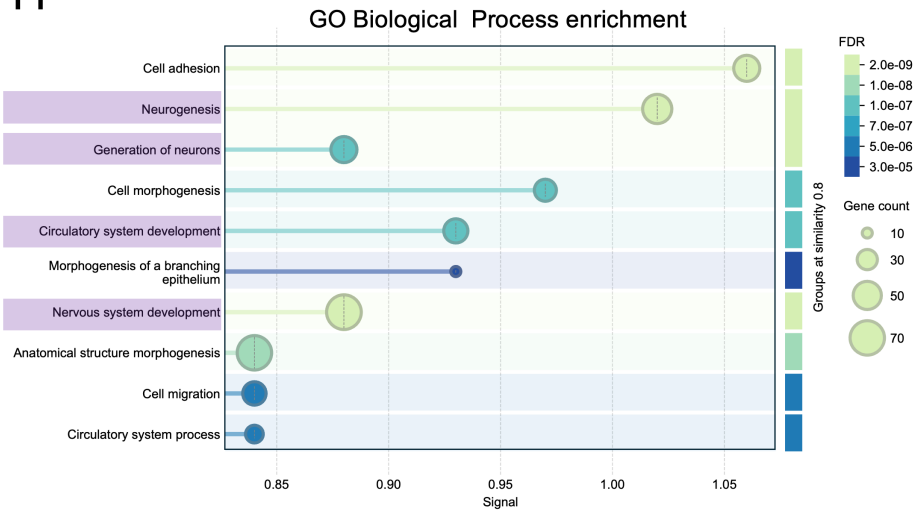

Figure4

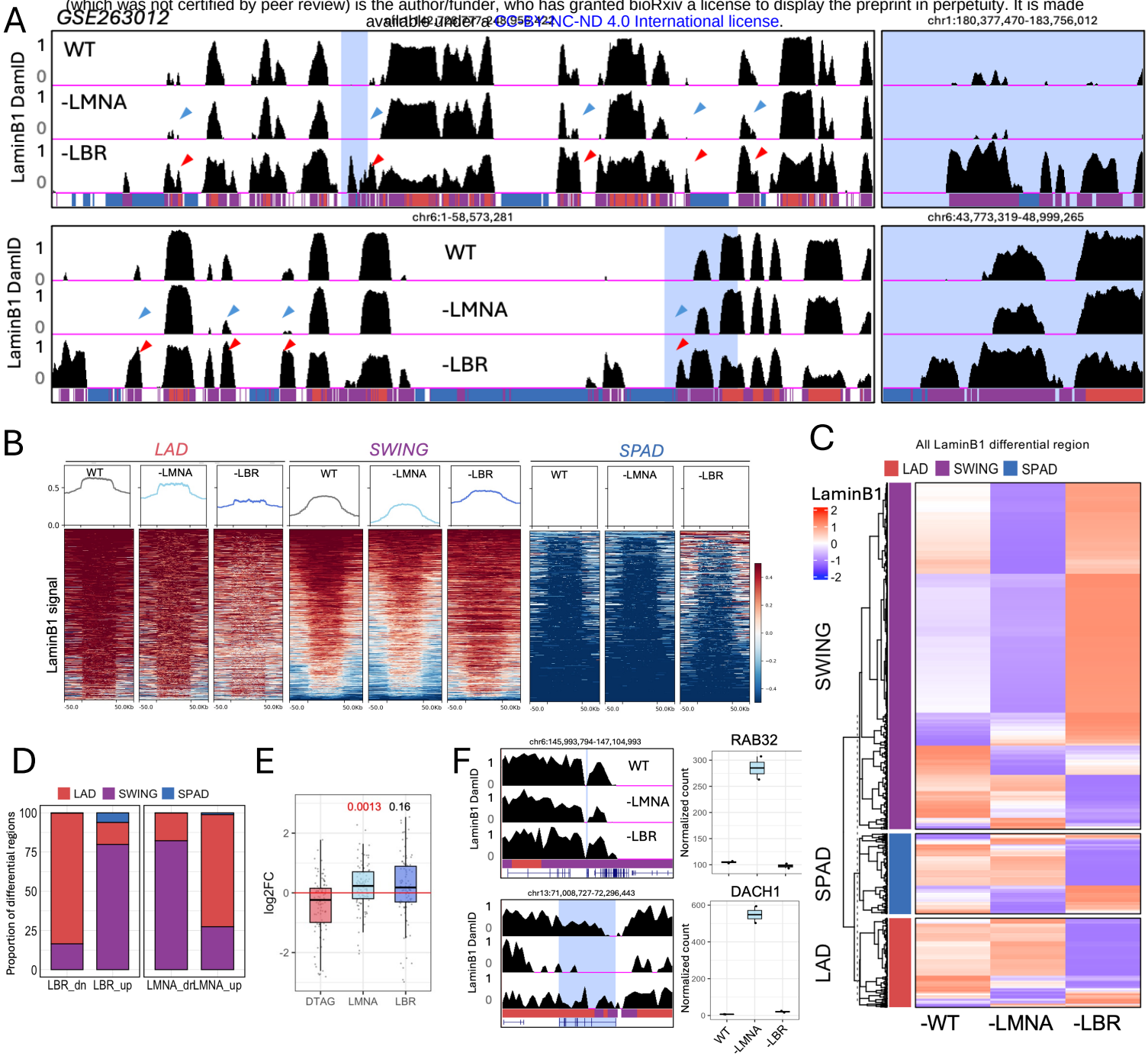

Figure5

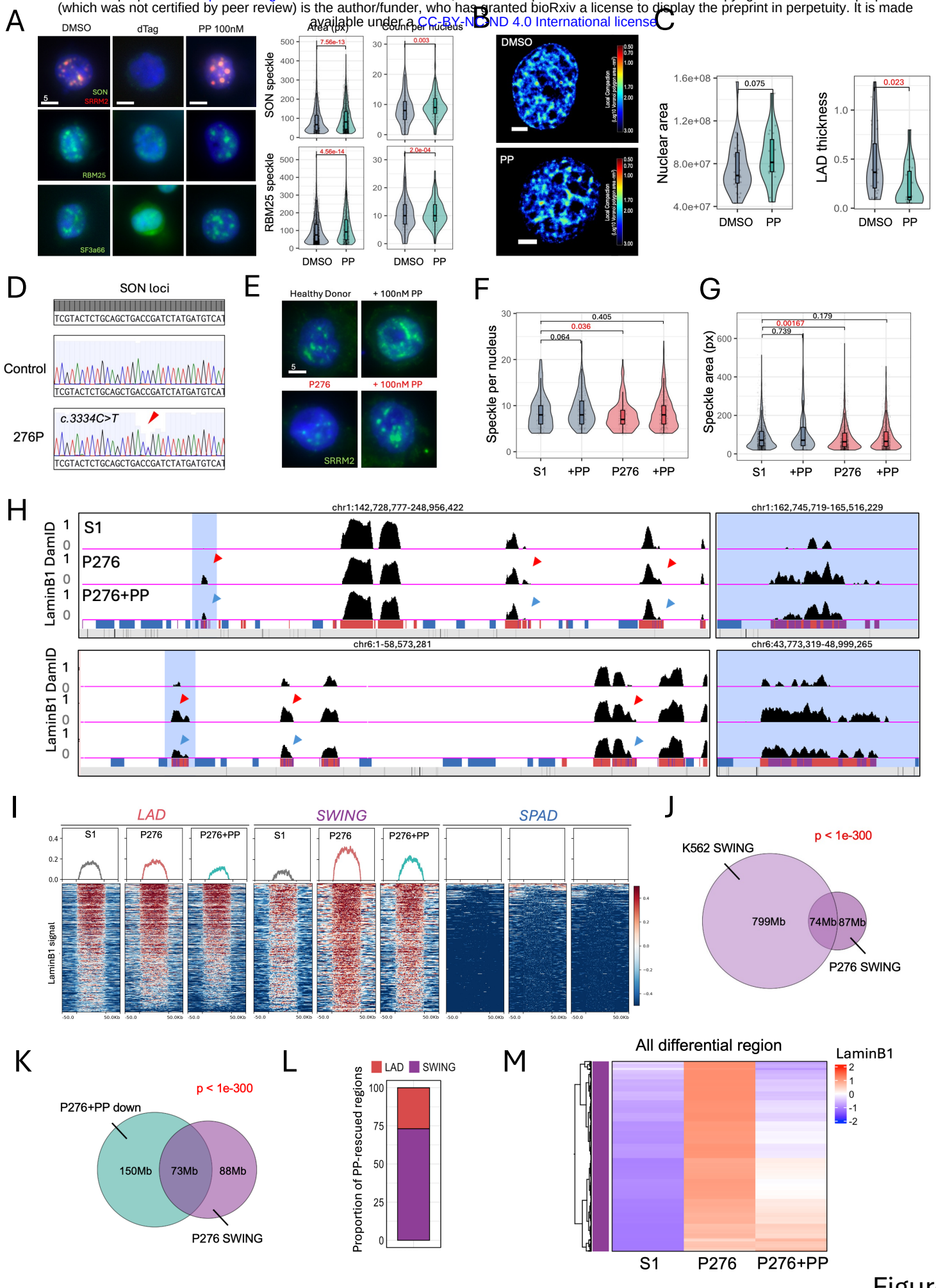

Figure6

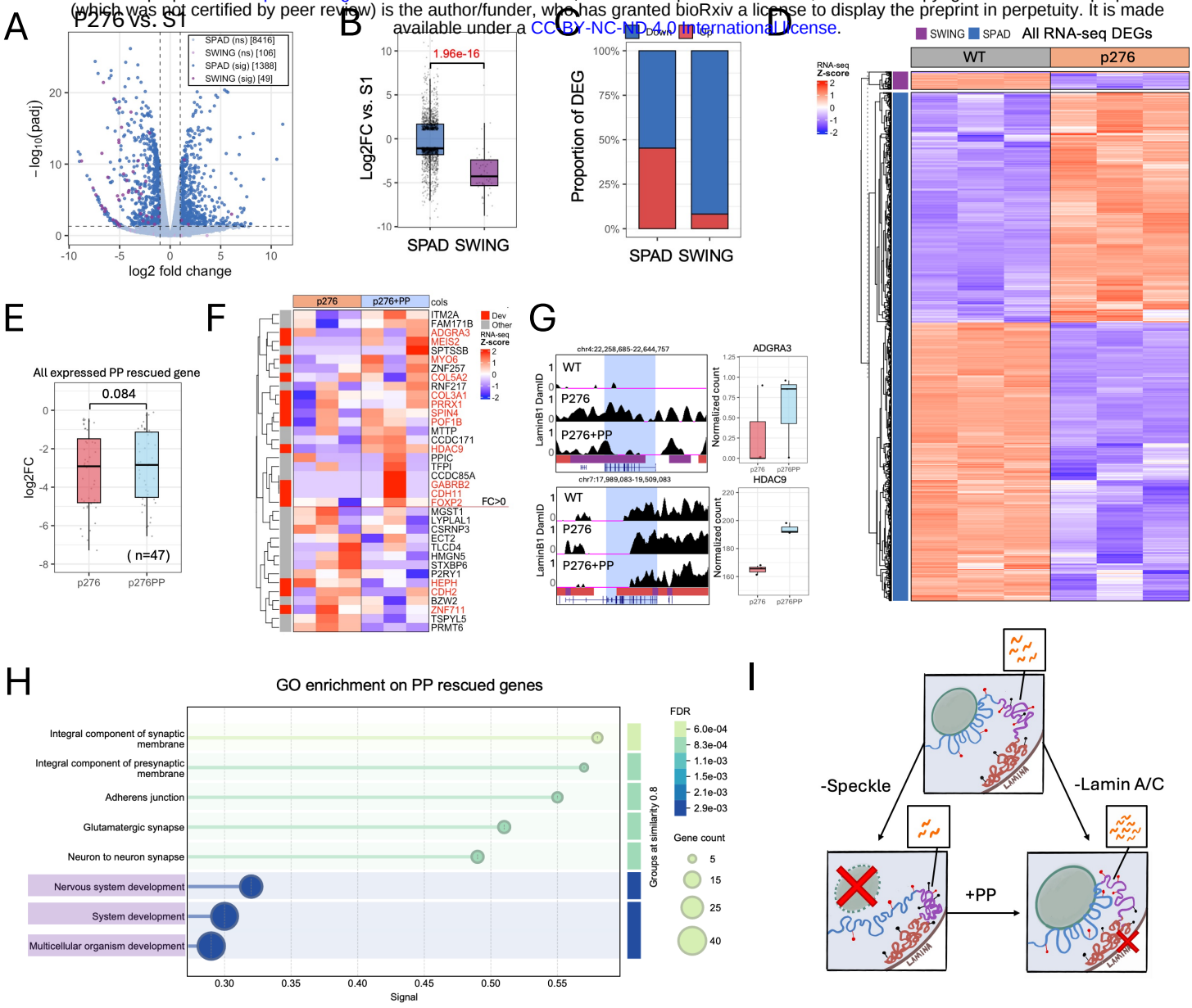

Figure7

A

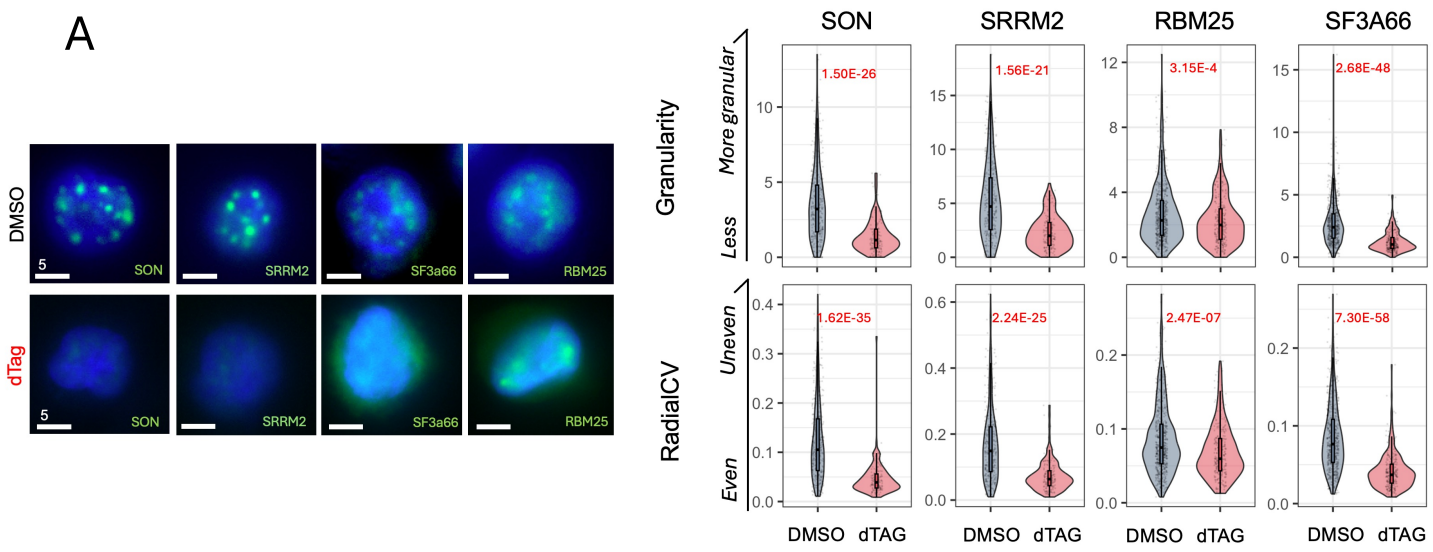

B

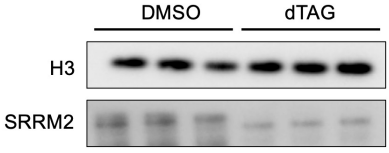

C

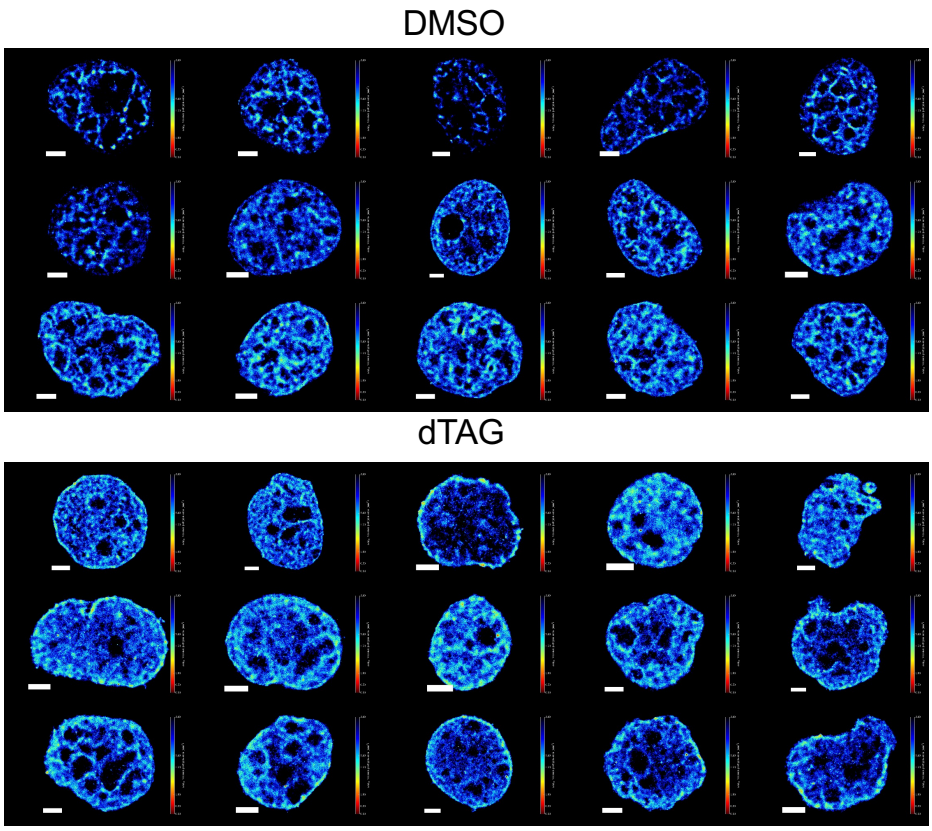

D

feature	DMSO	DTAG	fold_change	log2_fold_change	adj_p_value
log_periphery_dbscan_cluster_radius_skewness	0.369042	0.009705	0.026299	-5.24886	0.018444
log_interior_dbscan_cluster_spacing_skewness	-0.31398	0.014162	0.045103	-4.47063	0.037323
periphery_to_interior_dbscan_cluster_density_ratio	1.008075	2.045623	2.029238	1.020938	5.96E-05
log_model_lad_segment_thickness_mean	0.465918	1.493279	3.205027	1.680337	2.67E-13
model_lad_thickness	21.55336	120.1768	5.575781	2.479174	1.22E-10
periphery_dbscan_cluster_n_locs	21808.16	143518.4	6.580947	2.718295	9.93E-09

Supplementary Figure 1

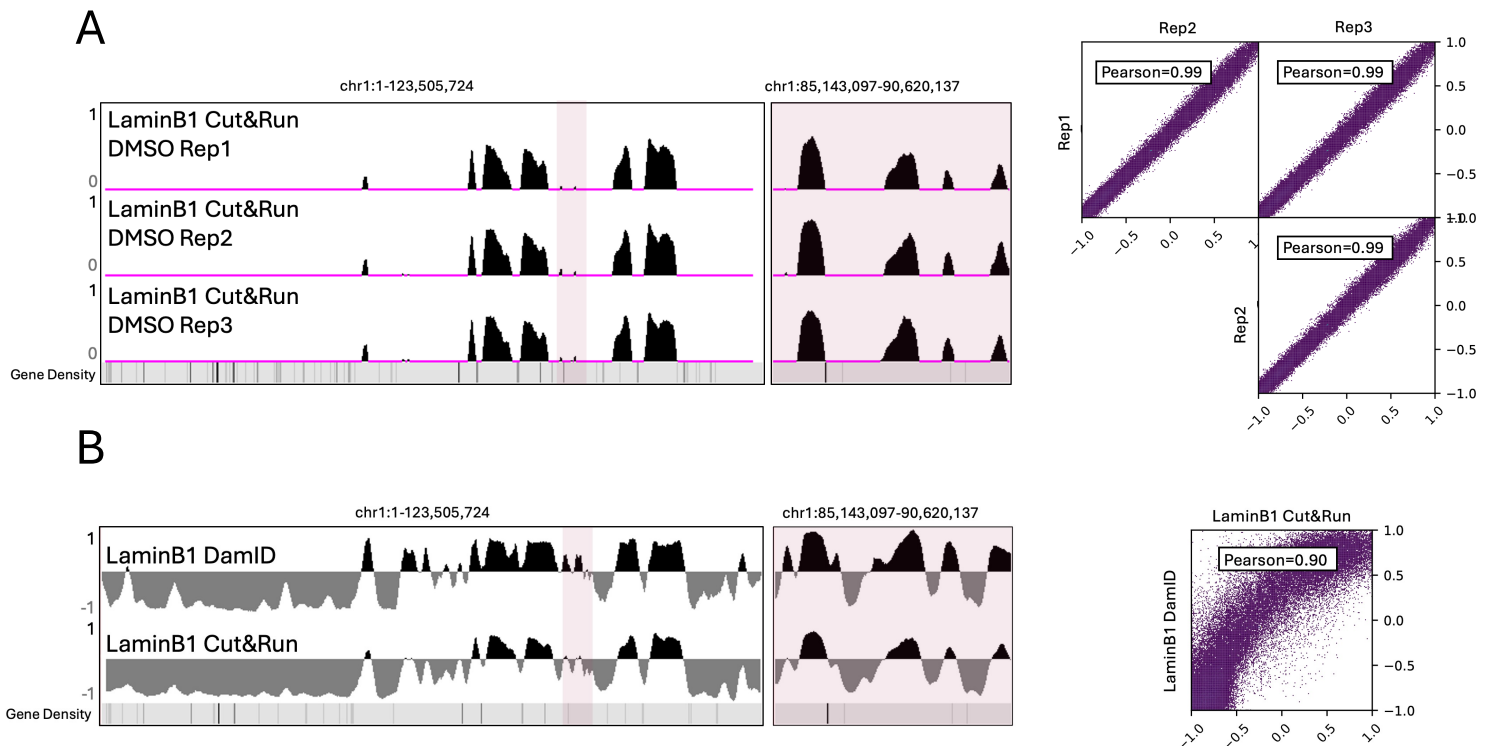

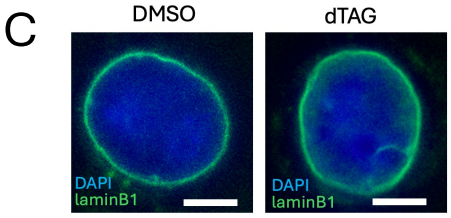

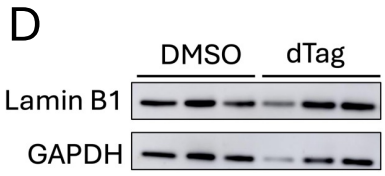

Supplementary Figure 2

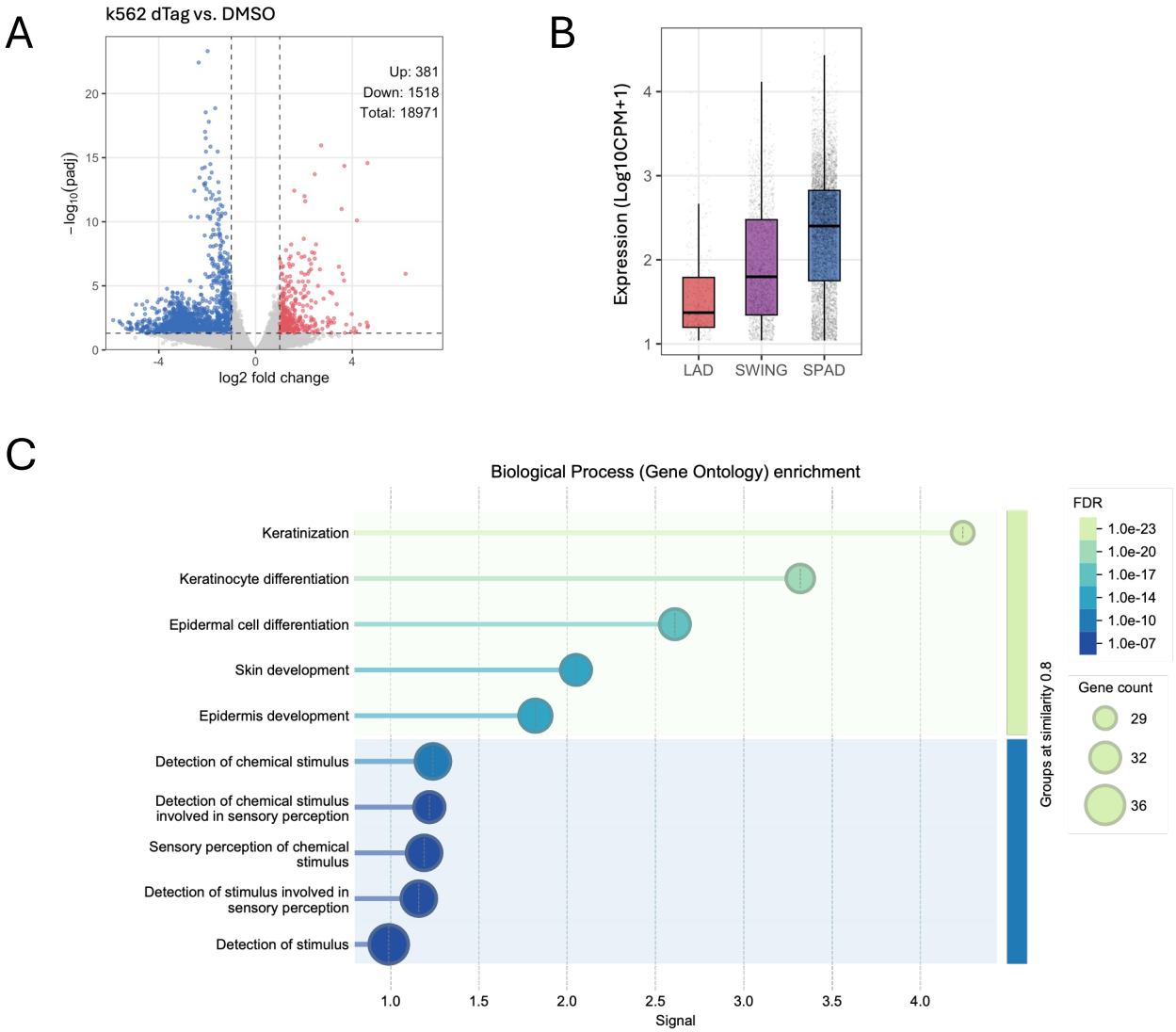

Supplementary Figure 3

A

RIMGC000276P (SON)

HP:0000639	Nystagmus
HP:0001252	Muscular hypotonia
HP:0002788	Recurrent upper respiratory tract infections
HP:0000565	Esotropia
HP:0002079	Hypoplasia of the corpus callosum
HP:0006956	Dilation of lateral ventricles
HP:0001263	Global developmental delay
HP:0004315	Decreased circulating IgG level
HP:0012430	Cerebral white matter hypoplasia
HP:0005216	Impaired mastication
HP:0000256	Macrocephaly
HP:0000403	Recurrent otitis media
HP:0002509	Limb hypertonia
HP:0001508	Failure to thrive

B

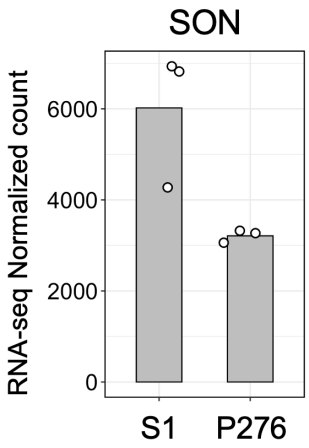

C

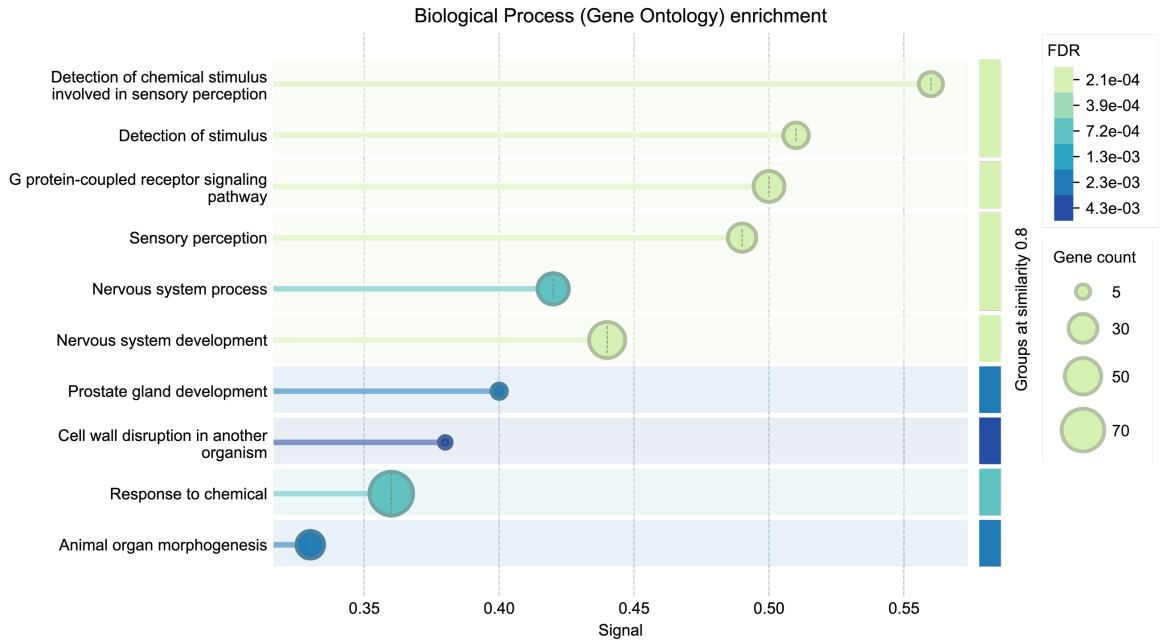

D

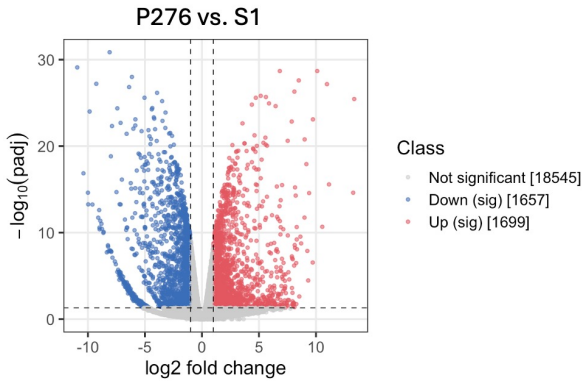

Supplementary Figure 4